UNIVERSITY OF CALIFORNIA,
IRVINE

Plasmonic Structures for the Control and Enhancement of Local and Remote Electric and Magnetic Fields at Optical Wavelengths

DISSERTATION

submitted in partial satisfaction of the requirements
for the degree of

DOCTOR OF PHILOSOPHY

in Chemistry

by

Brian Eugene Albee

Dissertation Committee:
Professor Eric O. Potma, Chair
Professor V. Ara Apkarian
Professor Matt D. Law

2017

DEDICATION

To

my family, my amazing wife, Genevieve, and friends

in recognition of their sacrifices and undying support

“Experience is merely the name men gave to their mistakes.”

Oscar Wilde

The Picture of Dorian Gray

TABLE OF CONTENTS

LIST OF FIGURES

LIST OF TABLES

ACKNOWLEDGMENTS

I would like to start by thanking my Ph.D. advisor, Dr. Eric O. Potma. Without the support and wisdom of Eric, I would not be where I am today. His kind, passionate, and patient style of leadership will always be a fond memory and set of lessons I carry with me for life. I also want to thank Dr. Ara Apkarian, for the amazing scientific insights and conversations, both scientific and not, you have shared with me. The kindness and wisdom I have gained wandering around with you and just talking will always stay with me throughout life. I thank my family (Mom, Dad, Grandma, Grandpa, and Kenny) for your support and sacrifices throughout life, it's always meant the world to me. From you, I have gained my persistent, free-spirit, unafraid to tackle the most challenging problems the world can throw my way. To my wife, Genevieve, the past six years would not have been the same without you. When things were stressful or tough you always were there, words can't express the appreciation and love I have for you. I thank Dr. Kim Edwards for the interesting opportunities developing teaching labs at UCI, these were always very enjoyable projects to work on. I thank all my colleagues in the Potma, Apkarian, and Capolino Labs, especially Alba, Kevin, Adam, Faezeh, Alex, Kate, Mahsa, and everyone else I just don't have enough space to mention (sorry!!!) for their friendship and support over the years. I will never forget the enjoyable times we all shared together in and out of lab, I wish you all the best in your future endeavors! To my best friends (Dave, Ian, James, Gene, Mohammed, the Kluns, and again those I can't fit here!!!), thank you for everything, it's been a fun ride so far, I miss you all! Finally, I would like to thank the DOE, NSF, and Keck Foundation for their financial support, without which, none of this work would be funded.

CURRICULUM VITAE

Brian Eugene Albee

2009-2010	Undergraduate Research Assistant, Bishnoi Group, Illinois Institute of Technology, Chicago
2010	B.S. in Chemistry, Illinois Insitute of Technology, Chicago
2010-2011	Research Technician, Bishnoi and Zasadzinski Groups, Illinois Institute of Technology, Chicago
2011-2017	Teaching Assistant, University of California, Irvine
2011-2017	Research Assistant, Potma Labs, University of California, Irvine
2017	Ph.D. in Chemistry, University of California, Irvine

FIELD OF STUDY

Plasmonic enhancement and control of electric and magnetic fields at optical wavelengths

PUBLICATIONS

1. **Brian Albee**, Kimberly Edwards, Eric O. Potma, "Simply SERS: A Teaching Lab for Honors and Majors General Chemistry Students," *In Preparation.* (2017).

2. **Brian Albee**, Xuejun Liu, Faezeh Tork Ladani, Rajen Dutta, Eric O. Potma, "Distance-dependent photo-induced electron transport in nanometer-sized junctions," *J. Opt.* 18, 054004 (2016).

3. Roie Knaanie, Jiri Sebek, Masashi Tsuge, Nanna Myllys, Leonid Khriachtchev, Markku Rasanen, **Brian Albee**, Eric O. Potma, R. Benny Gerber, "Infrared Spectrum of Toluene: Comparison of Anharmonic Calculations and Experiments in Liquid Phase and in a Ne Matrix," *In Preparation*. (2015).

4. Rajen Dutta, **Brian Albee**, Wytze E. van der Veer, Taylor Harville, Keith C. Donovan, Dimitri Papamoschou, Reginald M. Penner, "Gold Nanowire Thermophones," *Journal of Physical Chemistry C.* (2014).

5. C Cao, D Ford, S Bishnoi, T Proslier, **B Albee,** E Hommerding, A Korczakowski, L Cooley, G Ciovati, J F Zasadzinski, "Detection of Surface Carbon and Hydrocarbons in Hot Spot Regions of Niobium SRF Cavities by Raman Spectroscopy," *Physical Review Special Topics- Accelerators and Beams.* (2013).

6. Denise C. Ford, Charile Cooper, Lance D Cooley, Chad Thompson, Donald Bouchard, **Brian Albee,** Sandra Bishnoi, "Chemical Analysis of Fluorine in Niobium Electropolishing," *Journal of the Electrochemical Society.* (2013).

7. Jiri Sebek, Roie Knannie, **Brian Albee**, Eric Olaf Potma, R Benny Gerber, "Spectroscopy of the C-H Stretching Vibrational Band in Selected Organic Molecules," *Journal of Physical Chemistry A.* (2012).

8. Yibo Gao, Fei Liang, Gregory Freihofer, Benxin Wu, Bharathi Mohan, Seetha Raghavan, Jihua Gou, Shuyou Li, **Brian Albee,** Sandra Whaley Bishnoi, "Laser Sintering of Carbon Nanotube-Reinforced Ceramic Nanocomposites," *International Journal of Smart and Nano Materials.* (2011).

9. Ting Li, **Brian Albee,** Matti Alemayehu, Rocio Diaz, Leigha Ingham, Shawn Kamal, Maritza Rodriguez, Sandra Whaley Bishnoi, "Comparative toxicity study of Ag, Au, Ag-Au bimetallic nanoparticles on Daphnia Magna," *Analytical and Bioanalytical Chemistry.* (2010).

ABSTRACT OF THE DISSERTATION

Plasmonic Structures for the Control and Enhancement of Local and Remote Electric and Magnetic Fields at Optical Wavelengths

By

Brian Eugene Albee

Doctor of Philosophy in Chemistry

University of California, Irvine, 2017

Professor Eric O. Potma, Chair

In this thesis, we use plasmonic materials to achieve enhanced optical properties, including the enhancement of Raman scattered light, the enhancement of optically induced electron tunneling, and the enhancement of the magnetic field component of light interacting with matter.

Our first focus is the development of a teaching lab, which introduces the concept of Surface Enhanced Raman Scattering (SERS) to students in general chemistry lab settings. In the lab, students synthesize gold nanoparticles and perform Raman measurements, examining the concentration dependent spectrum of thiocyanate in aqueous solution with and without gold nanoparticles. Through this experience, students learn the chemical and physical foundations of SERS measurements in a simple, elegant manner. This helps students recognize the capabilities and fundamentals of advanced Raman spectroscopy, a topic often underrepresented in chemistry teaching labs.

Next, our focus is shifted to the fabrication of devices to generate rectified currents upon illumination. The rectifying element is a nm-sized slit between two gold electrodes. Dc current is produced upon illumination due to asymmetries in the junction. Such photo-induced currents are enhanced by surface-plasmons in the nanogap, excited by remote surface plasmon polaritons (SPPs) launched 10 microns from the gap. We describe the fabrication of nanogaps ranging 4-20nm in size in Au bowties using a combination of Focused Ion Beam (FIB) and electromigration techniques. We observe SPP-driven electron tunneling events in the devices, elucidating the natural transition of Tien-Gordon type tunneling into Fowler-Nordheim field emission with increasing illumination power, and demonstrate that these two mechanisms have similar physical origins.

Finally, we describe the use of surface plasmons to enhance and control the interaction between the magnetic field component of light and matter. To do so, we fabricate and explore plasmonic Au nanostructures designed to enhance local magnetic fields at optical wavelengths. The tunability of the device is described as a function of gap size. In addition, we propose a method for optically probing enhanced magnetic fields generated in the devices using trivalent lanthanide ions. Finally, we discuss scattering experiments on a single Er_2O_3 nanoparticle illuminated with azimuthally polarized light, indicating the possible involvement of a magnetic resonance near 800nm.

CHAPTER 1: Introduction

A plasmonic material exhibits a collective electron cloud oscillation upon illumination. Among materials that have been widely researched and that exhibit this unique property, gold nanoparticles and materials (AuNPs) have become especially notable. This is due to the presence of plasmon resonances in the visible range of the spectrum for these particles. The plasmon resonances give rise to the characteristic color of the gold nanoparticles.

In the near field, plasmonic resonances give rise to enhanced local fields, opening opportunities for forms of enhanced spectroscopy. For instance, if a molecule is bound to such an AuNP, the enhanced field allows for the enhancement of Raman scattered light as well. As a result, very small concentrations of Raman active molecules can be measured spectroscopically using this technique [1].

While molecules can be bound to the outside of singular gold nanoparticles to achieve surface enhanced Raman scattering, molecules can also be chosen which allow controlled aggregates of AuNPs to form in solution. The binding of two AuNPs with a molecule allows for the construction of tailored nanoantennas. When light is introduced into the junction of a nanoantenna, bound together by a molecule, the electric field of the light is amplified and focused tightly between the particles making up the nanoantenna dimer or multi-particle aggregate. If the molecule in the hotspot of the antenna is Raman active, Raman spectra can be acquired from only a few molecules, down to the single molecule level [2]. In doing so, the diffraction limit of light is broken, permitting a new level of precision in chemical analysis. This

principle can easily be demonstrated in the lab by binding a molecule such thiocyanate to AuNPs in colloidal solution and performing a quick Raman measurement (Chapter 2).

While such feats are interesting, much more can be done with plasmons beyond chemical detection. As efficient energy sources and devices have become critical to society, light to energy conversion materials have become a key focus for researchers worldwide. While traditional research in these materials is often based on semiconductors, plasmonic materials made with noble metals (Au, Ag, Cu) offer interesting new ways of converting light into usable electron currents as well. An example of this is given in Chapter 3, where, Au thin-films, as opposed to particles, are used to support a propagating surface wave, known as a surface plasmon polariton (SPP) It has been demonstrated that these remotely launched surface waves can be used to excite molecules and particles [3]. It remains a challenge to convert SPP energy into a device that is based on controllable light-to-energy conversion using Au thin-films. In Chapter 3, we use light-driven tunneling across plasmonic nanoscale gaps as a mechanism for light-to-energy conversion, an approach that allows for interesting possibilities in the design and powering of the next generation of plasmon-based electronics [4].

While most research into Au nanomaterials deals with the enhancement and control of electric fields, as well as applications using said phenomena, the enhancement of the magnetic component of light has historically been of great interest to researchers as well. Despite this, optical magnetism has remained a curiosity rather than becoming a widespread technique used throughout science and engineering.

Generally, it is known that the interaction of the magnetic field of light with matter is many orders of magnitude weaker than the interactions with the electric field component. As a

result, performing spectroscopic measurements with the magnetic field component or the designing feasible devices using magnetic field interactions has largely eluded researchers to date. Despite these challenges, it has been demonstrated that nanoscale Au resonators can be fabricated that enable enhancement of magnetic fields at optical wavelengths (Chapter 4). To benefit from magnetic light-matter interactions, enhancement of optical magnetism effects is needed. This can be achieved with specially designed plasmonic nanoantennas In Chapter 4, we discuss the design and fabrication of nanoantenna systems that can be used to enhance magnetic optical field interactions. In addition, we will highlight a method to measure the local magnetic fields with the aid of materials that contain trivalent lanthanide ions [5, 6].

In this dissertation, we will explore the enhancement and control of electric and magnetic fields as described above in Au nanomaterials. To explore the enhancement and control of local electric fields associated with an illuminated particle, will we will introduce a SERS teaching lab developed to teach the very basics of field enhancement and plasmons (Chapter 2) [7]. To demonstrate the conversion of light to useable energy in plasmonic materials, we will focus on the launching of remote SPP modes to drive electron tunneling events in nanoscale gaps [4] and Two Photon Electroluminescence (TPEL) in CdSe:ZnS quantum dots (Chapter 3). Finally, we will explore ways to enhance and control the magnetic field of NIR light using plasmonic Au nanostructures and trivalent lanthanide reporters (erbium triflate and neodynium triflate), as well as study the optical magnetism of Er_2O_3 nanoparticles (Chapter 4).

References

1. M.D. Sonntag, J.M. Klingsporn, A.B. Zrimsek, B. Sharma, L.K. Ruvuna, R.P. Van Duyne, "Molecular plasmonics for nanoscale spectroscopy," Chem. Soc. Rev. 4 (2014).

2. S. Yampolsky, D.A. Fishman, S. Dey, E. Hulkko, M. Banik, E.O. Potma, V.A. Apkarian, "Seeing a single molecule vibrate through time-resolved coherent anti-Stokes Raman scattering," Nature Photonics. 8, 650-656 (2014).

3. X. Liu, Y. Wang, E.O. Potma, "A dual-color plasmonic focus for surface-selective four-wave mixing," Appl. Phys. Lett. 101, 081116 (2012).

4. B. Albee, X. Liu, F.T. Ladani, R.K. Dutta, E.O. Potma, "Distance-dependent photo-induced electron transport in nanometer-sized junction," J. Opt. 18, 054004 (2016).

5. R. Hussain, S.S. Kruk, C.E. Bonner, M.A. Noginov, I. Staude, Y.S. Kivshar, N. Noginova, D.N. Neshev, "Enhancing Eu^{3+} magnetic dipole emission by resonant plasmonic nanostructures," Opt. Lett. 40, 1659-1662 (2015).

6. M. Kasperczyk, S. Person, D. Ananias, L.D. Carlos, L. Novotny, "Excitation of Magnetic Dipole Transitions at Optical Frequencies," Phys. Rev. Lett. 114, 163903 (2015).

7. B. Albee, K.D. Edwards, E.O. Potma, "Simply SERS: Experiment for General Chemistry Laboratory," J. Chem. Educ. In Submission (2017).

CHAPTER 2: Simple SERS Experiments for the General Chemistry Teaching Lab

2.1 Background and significance

Surface enhanced Raman Spectroscopy (SERS) has become a popular analysis tool, because of the exciting promise the technique has shown for bringing chemical sensing and imaging methods to new levels of sensitivity. By using SERS to focus light to nanoscopic probing volumes, a plethora of research in the field has led to a better understanding of how to control and enhance electromagnetic fields. Examples of SERS based technology in the literature lays bare a wide range of scientific capabilities that are difficult to explore with traditional spectroscopic tools.

SERS based technology has allowed researchers to push the limits of detection for biologically relevant molecules, for instance, the detection of low concentrations of chemicals associated with cancer diagnosis [1-3]. In addition, dimers of gold and silver nanoparticles have allowed single-molecule Raman spectroscopy and nonlinear Raman spectroscopy methods [3-6]. SERS is changing the capabilities that researchers have at their disposal to investigate materials and chemicals.

Despite the many STEM related fields that may benefit from SERS, from engineering to physics, there are not many examples of SERS teaching tools available that introduce university students to SERS based technologies in academic settings. With better tools, we can inspire a new generation of scientists to develop the technology of tomorrow using SERS principles. There are few examples in the literature of SERS based teaching labs geared towards

introducing this advanced concept to undergraduate students [7]. However, most of these labs are intended for students enrolled in advanced chemistry labs, which are not taken by all STEM students [8-10].

As a result, only a small community of undergraduate students is typically exposed to SERS based technologies on a yearly basis. Even fewer end up pursuing research in the topic, and unfortunately most experience and conceptual knowledge about SERS for undergraduate students in STEM based education fields comes solely through research lab exposure. If a wider STEM student population could be exposed to SERS in an effective way earlier, it might inspire students to work with SERS based technology that further advance our control and manipulation of light for generations to come.

To rectify this lack of exposure, we present a novel teaching lab for undergraduate students that allows for a simple introduction to SERS. In addition, we will explore a variety of focus points that can be highlighted and expanded on as follow up labs exploring more intricate aspects of SERS from an observational standpoint, allowing for a broad introduction of SERS into a variety of different lab settings including and not limited to general chemistry, physics, and engineering academic curriculums [11].

2.1.1 Light Scattering and the Raman Effect for Students

To teach the greater concept of SERS to students, communicating the fundamentals and basics of light scattering and the application to Raman spectroscopy in a simple and effective way is key. The scattering of light off a medium can be broken down into two key categories: elastically scattered light and inelastically scattered light. This concept is demonstrated in figure 2.1. Here we show the absorption of light by a molecule or particle excited by a single

wavelength or frequency. As is demonstrated, there may be an elastic scattering event, known as Rayleigh scattering. This is where the energy of emission or scattering by the excited molecule or particle is equivalent in energy, i.e. Delta E = 0. However, light scattered by the molecule may also gain or lose energy, a process known as the Raman effect. If the difference in energy is resonant with a vibrational energy level or other physical process such as electron cloud oscillation, Raman spectroscopy and SERS techniques may be explored further. The next section will expand upon the connection of inelastic scattering, particularly Stokes scattering, and how it is applied to obtaining the vibrational spectrum of molecules of interest.

Figure 2.1: Jablonski diagram showing the physical mechanisms of elastic and inelastic scattering processes. In Raman and SERS measurements, typically anti-stokes scattering is monitored. If the difference in energy between the excitation photon, and the red-shifted photon that is scattered back is resonant with a vibrational excitation in a molecule, a Raman spectrum can be obtained for such a scattering event.

2.1.2 Raman Spectroscopy

As we have described previously, when light is scattered that has lost energy an event called a Stokes shift occurs, meaning the observed photon is red shifted from the initial color of light used to excite the system. If the difference in energy between the excitation photon and scattered photon is resonant with a vibrational energy level in a molecule or particle, a Raman spectrum can be measured. Raman spectroscopy has proven to be especially useful in modern chemistry and physics due to its potential for measuring the vibrational spectrum of a wide range of materials in solid, liquid, and gas environments. This has allowed Raman spectroscopy to find a home in many research labs ranging from biologically relevant chemical sensing studies, to art and archeology analysis [12-14]. Despite this wealth of knowledge, to truly achieve the state of the art in chemical sensing, Raman spectroscopy not only needs to be able to be used for identifying chemicals, but pushing the detection limits to the next level. Typically, Raman measurements will allow for the detection of molecules with modern instrumentation down to the uM-mM range. To achieve spectroscopic sensitivity at the nM to single molecule level, Raman spectroscopy alone cannot get the job done. To push measurements to these limits, the light field interacting with the system must be amplified, as well as focused much tighter than the diffraction limit of light to measure the signal from a single molecule. This is where an optical trick called Surface Enhanced Raman Spectroscopy comes into play. As we move to the next section, we will explore how SERS can be used to amplify the field of light a molecule or particle sees as well as focus that light in such a way that spectra can be detected from low concentrated samples in the nM range down to the single molecule level.

2.1.3 Surface Field Enhancement

To achieve the detection limits needed to do measurements with sensitivity down to the single molecule limit, a specialized optical trick known as Surface Field Enhancement can be used to enhance the optical fields needed to reach this level of sensitivity. To do this, a special set of materials known as plasmonic materials are used.

Plasmonic materials can be defined as materials with a collective electron oscillation that is resonant at a certain frequency. Gold nanoparticles are an example of a popular plasmonic material, and is the basis for SERS measurements in this teaching lab experiment set as well. In the case of gold nanoparticles, this collective electron oscillation typically occurs at optical frequencies of light ranging from 500-800nm, wavelengths that are easily, and affordably detected with modern spectrometers. If light is sent to interact with this particle that is resonant with the surface plasmon oscillation frequency, the field of this light is locally enhanced. In addition, the amplified field is confined to the near field, extending from the surface of the particle at the nm scale. The control and enhancement of this field allows us to go one step further, serving as the basis for single molecule scale spectroscopic measurements.

2.1.4 Surface Enhanced Raman Scattering (SERS)

Now that we have discussed the amplification of scattered light fields using plasmonic materials such as gold nanoparticles, we can finally make the connection to Surface Enhanced Raman Spectroscopy. If a molecule of interest at low concentration (nM) is bound to that particle with Raman active modes, the amplified field allows for the detection of previously undetectable amounts of analyte compared to standard Raman measurements. If a molecule is chosen that can bind together particles as dimers and trimers, the enhanced field can be

focused between multiple gold nanoparticles, which act as electric field antennae, to yield single molecule level spectroscopic measurements. This principle is demonstrated in Figure 2.2.

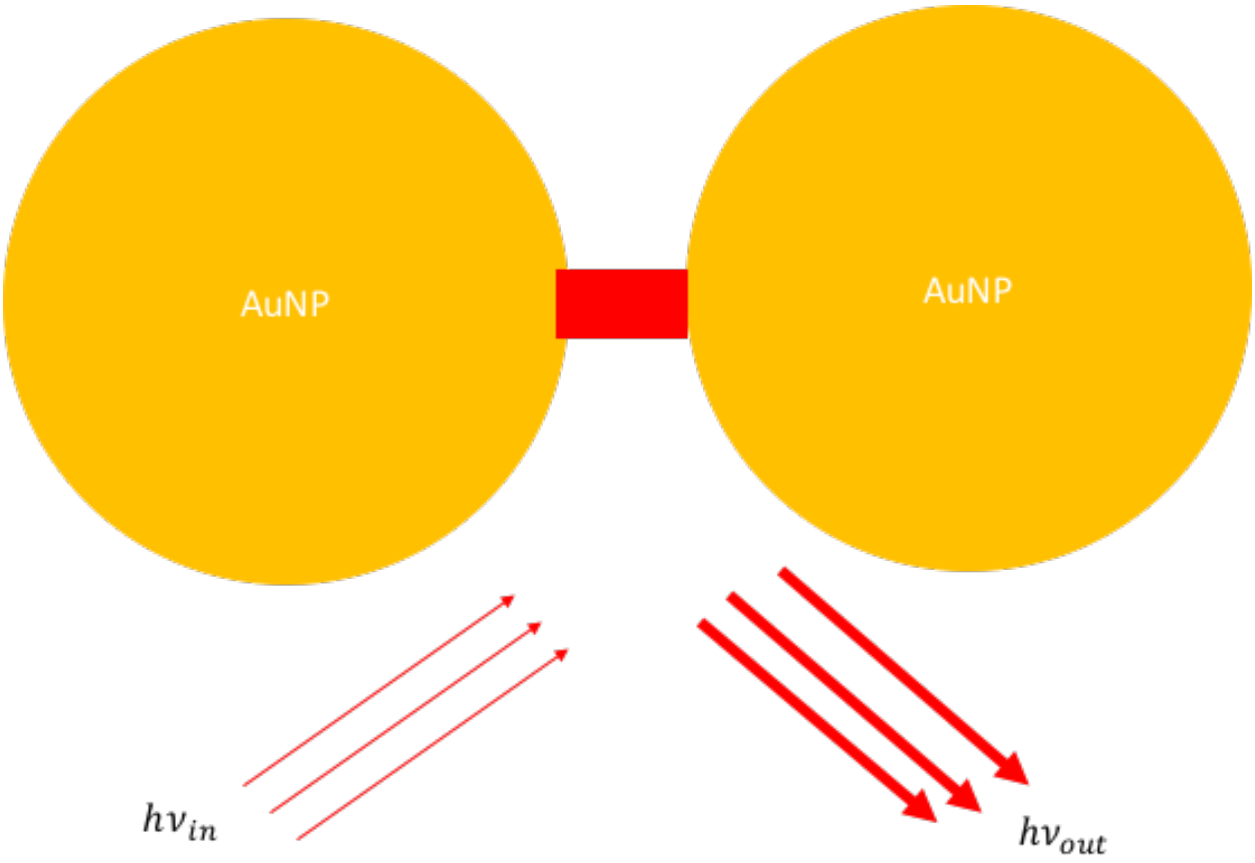

Figure 2.2: Surface Field Enhancement of AuNPs acting as electric field antenna. As shown in the diagram, the oscilation of the field between the particles enhances the signal scattered from the optical antenna. If a molecule is placed in this junction that binds the particles together, such as thiocyanate, a surface enhanced raman measurement can be performed in solution that allows for identification of the cyanide stretch in a SERS teaching lab procedure for undergraduate general chemistry teaching courses.

2.1.5 Vibrational Spectroscopy of Thiocyanate using SERS

To perform SERS measurements, a good candidate molecule is a key ingredient to the process. This is because of the need for binding a molecule of interest to the surface of plasmonic particles to perform such measurements. Chemically speaking, thiols and nitrogen containing chemical groups such as cyanide are well known to interact with gold in such a way as to bind to the surface of gold nanoparticles, forming a self-assembled monolayer around the particles in solution. As a result, thiocyanate can be expected to bind to gold nanoparticles in solution in such a way to produce a SERS active substrate that can be easily explored in an academic teaching lab setting. The following experimental section of this chapter will detail the exact procedure of nanoparticle synthesis and Raman measurements used by the students to perform SERS measurements of thiocyanate, as well as their expected observations. The binding of this molecule to a gold nanoparticle is further demonstrated in Figure 2.3.

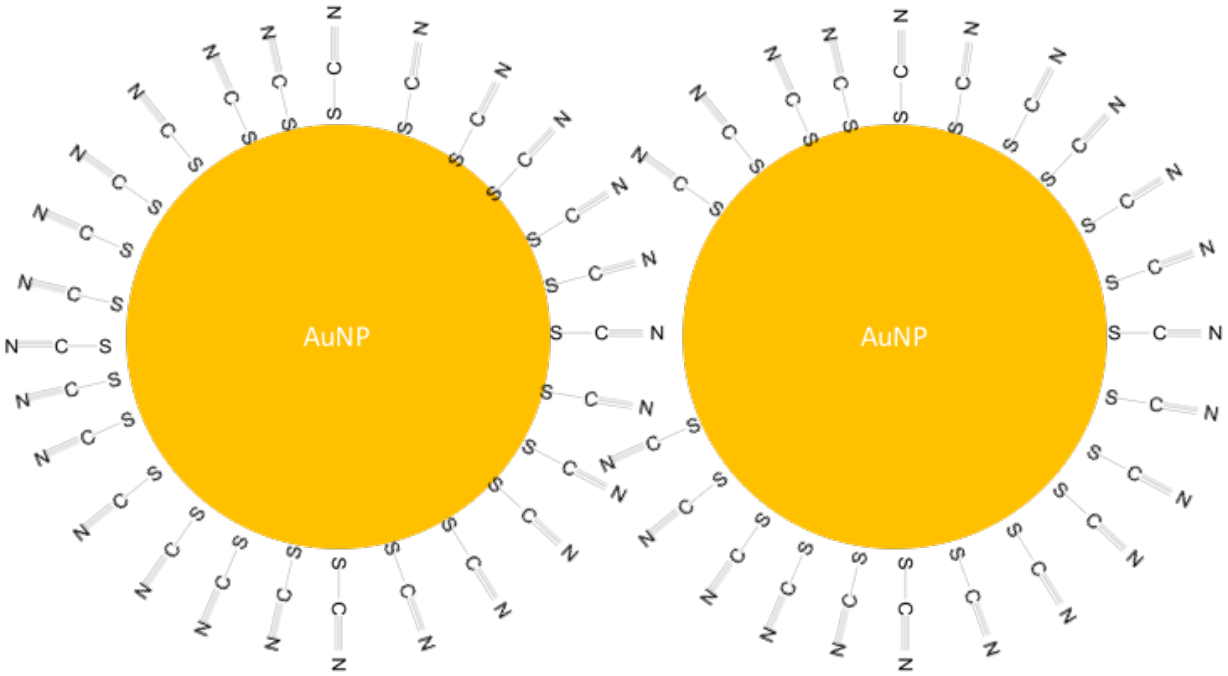

Figure 2.3: The binding of thiocyanate to AuNPs in solution to form SAMs that cover particles and cause aggregate formation in solution, including dimers, trimers, and other larger clusters of AuNPs. These aggregates act as electric field antenna under illumination, enhancing the field between particles making up the clusters. When Raman measurements are performed using these aggregates, SERS measurements can be taken ranging from single molecule precision on glass substrates up to nM concentrations in solution.

2.2 Experimental

2.2.1 Incorporating the Model Observe Reflect Explain (MORE Approach)

To perform this lab, students follow a template called the Model, Observe, Reflect, Explain approach. To do this, students are given a set of prelab lecture slides that explain the concepts of Vibrational Spectroscopy, Raman scattering, and Surface Enhanced Raman Spectroscopy. They are asked to hypothesize what will happen when they observe the Raman spectrum of SCN in various concentrations, as well as when exposed and bound to the surface of a plasmonic material, gold nanoparticles. Upon answering these prelab questions, students perform the lab and make observations as they perform the procedure. The students are expected to adapt their hypothesis model as they perform the lab. After completion, the students reflect on their work by answering a series of post lab questions related to their prelab and observations. Finally, the students reflect by revising their original hypothesis to fit their observations and writing a short paragraph about what they have learned with respect to SERS.

2.2.2 Synthesis of Colloidal Gold Nanoparticles

To perform the in-lab portions of the experiment, students are first required to synthesize gold nanoparticles using an adapted sodium citrate reduction method [15]. This is performed by placing .3mL of 1% chloroauric acid solution into 20mL of boiling nanopure water. .2mL of 2% sodium citrate is added into the solution to reduce the gold into a ruby red solution of gold colloid. Once synthesized, the students allow the colloid to cool to room temperature before running any Raman measurements focused on the particles. DLS measurements of the

particles indicated a diameter of 20nm, with a consistent Polydispersive Index (PDI) of .995 or above using this synthesis.

2.2.3 SCN- Raman Measurements in Solution

While the synthesized gold nanoparticles cools, students perform measurements on a series of SCN- standards to understand the detection limits of Raman spectroscopy. Students first take the spectrum of a 2M KSCN standard to see the cyanide stretch of the molecule in solution. Once this is complete, the students produced a ~1uM solution barely detectable by Raman by placing 6 drops of 2M KSCN into a 2mL cuvette of nanopure water. The difference in intensity of the peaks allows students to visually understand the concentration dependence of a Raman active sample in a straightforward, yet elegant manner.

2.2.4 SERS Measurements of SCN- in Solution

To perform the SERS measurements, students first take a Raman spectrum of the gold nanoparticles synthesized in the first part of the experiment to determine the spectral contribution, or lack thereof, for the gold nanoparticles in the cyanide stretching region. Once finished, the students add 6 drops of 2M KSCN to a cuvette filled with the gold nanoparticles they synthesized. They observe a color change from red to violet in the colloid as the SCN binds to the surface of the particles, and causes aggregates including dimers and trimers, to rapidly form in solution. This color change observation is detailed in Figure 2.4. Immediately after observing this color change, the students record the SERS spectrum of the thiocyanate bound to the surface of the gold molecules. This observation allows students to see first-hand how

the enhancement of excitation fields allows for the detection of concentrations of molecules much lower than standard Raman measurements allow for.

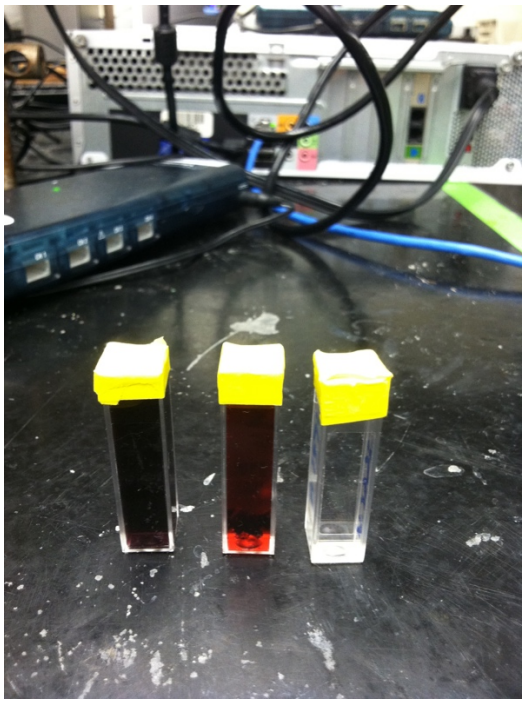

Figure 2.4: Representative image of cuvettes prepared using the developed teaching lab. The clear solution to the right is a 2M KSCN standard. The red cuvette shown in the middle is filled with AuNPs synthesized according to the procedure detailed in this chapter. The final cuvette on the left is filled with AuNPs with 6drops of 2M KSCN added into the cuvette prior to Raman analysis. As we can see, a distinct color change occurs as the thiocyanate binds to the AuNPs in solution forming dimers, trimers, and larger aggregates that can be used to perform SERS measurements in solution.

2.3 Results and Offshoot Experiments

2.3.1 Student Trial Success Rates

Overall, roughly 300 students performed this experiment as a trial during the Winter quarter of 2017 at UCI in the honors and majors' general chemistry lab course. About 66% of the students that performed the lab could do so to completion. Contaminated glassware interfered with the synthesis of student nanoparticles in the largest number of cases of failure, yielding particles not capable of producing good SERS signals at the excitation wavelength used, 785nm. Of the students that achieved successful particle synthesis, about 90% could achieve significant SERS measurements when adding SCN- to the colloid. Those who did not get good particles or spectra were given a sample prepared by the teaching assistant to obtain data for their analysis. In the post lab analysis, roughly 33% of the students could identify the process of SERS, and make a connection to how SERS can be used to amplify the signal of a molecule at a concentration not normally detectable by standard Raman measurements.

2.3.2 Additional Experiments

A representative spectrum, as well as the setup used by the students to acquire the measurements by the students for each sample during the laboratory procedure is detailed in Figure 2.5. As we can see here, an additional observation can be made by the students as well beyond the simple SERS observation focused on in this version of the experiment. While the thiol group is traditionally used to bind molecules to gold particles, the added binding interaction of the cyanide group in the thiocyanate molecules allows for the formation of particle aggregates in solution. As a result, a shift in the cyanide stretch occurs, and is now

measured at a higher frequency than unbound $^{-}$SCN. The expected Raman shift of the cyanide stretch in unbound $^{-}$SCN in aqueous conditions is seen at 2050cm^{-1}. After reacting with gold nanoparticles to form aggregates in solution, the cyanide stretch is now seen at 2150cm^{-1}. This allows an easy off-shoot experiment to be performed, or questions added by an instructor, to include observations about the frequency shift due to the interaction of cyanide with gold nanoparticles in solution, and the aggregates formed that allows for this observation.

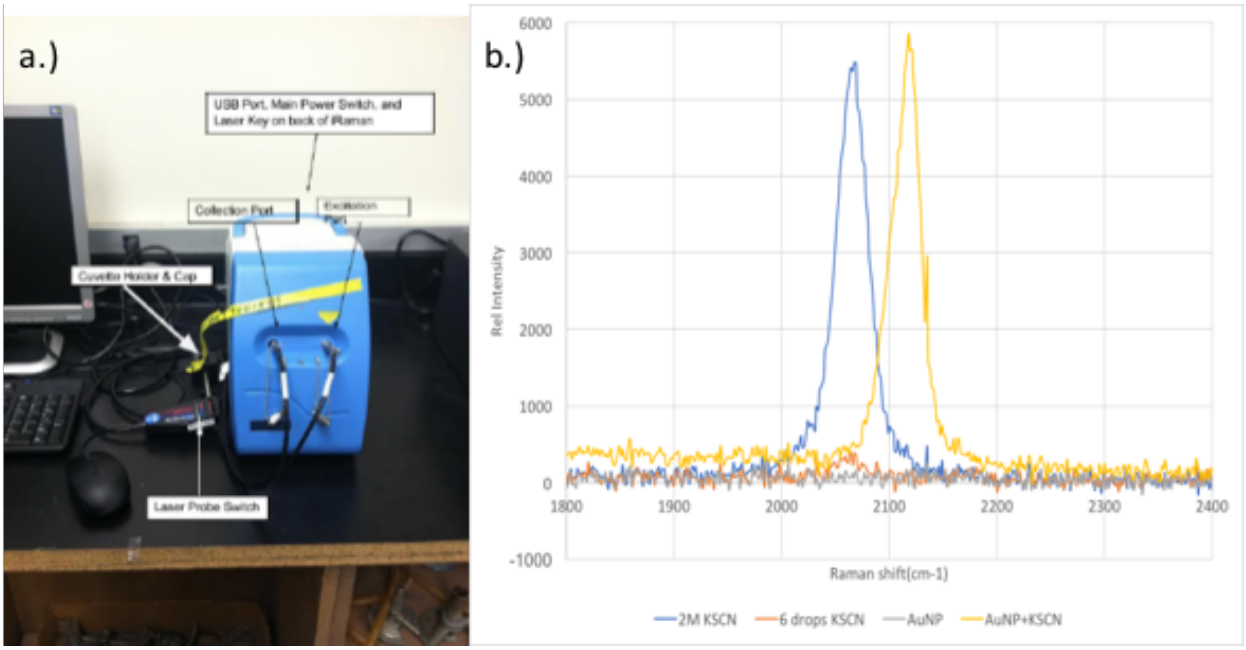

Figure 2.5: a.) The setup of the Raman spectrometer used by students to perform Raman measurements. In this set of experiments the students used a BWTEK iRaman equipped with a 785nm laser built into the portable spectrometer. Cuvettes were held in a holder provided by BWTEK that allowed connection of a fiber optic probe that can be used for excitation and collection of spectra directly in the cuvette samples. A representative set of spectra acquired using the procedure is shown in b.). As we can see, the 2M and low concentration samples of KSCN give a concentration dependent peak at 2050cm^{-1}, while the SCN- bound to AuNPs give a strong SERS response at 2150cm^{-1}. The shift in the cyanide stretch to a higher frequency is a result of the cyanide binding AuNPs in solution to form dimers, trimers, and other larger aggregates.

2.4 Concluding Remarks

In this chapter, we have demonstrated a SERS teaching lab for general chemistry laboratory settings. In this lab, students answer a series of prelab questions and formulate hypotheses related to their SERS experiment as prescribed by the MORE approach. After finishing these prelab questions, students perform the SERS lab procedure and adjust their original hypothesis as they make observations throughout the lab. During the in-lab portion of the experiment, students synthesize gold nanoparticles using a citrate reduction reaction, and perform a series of Raman measurements using the gold particles and thiocyanate to explore basic concepts of SERS hands-on. Upon completion of the lab, students answer a series of post-lab questions connecting the concepts of SERS learned in the classroom prior to the in-lab experience and observations collected. This teaching lab has been tested in a general chemistry lab setting at the University of California Irvine in the Winter quarter of 2017, with roughly 300 performing the experiment during the trial. 66% of students could successfully grasp the concepts of SERS from this lab. As a result, we have demonstrated a simple, adaptable experiment that allows for student exposure to the advanced research topic of SERS, in a simple, elegant manner. By introducing advanced concepts such as SERS to students at an earlier age in an adaptable way, we can inspire and prepare even greater numbers of students to push the boundaries of research with respect to this emerging field of research and achieve the next-generation of technology through their own academic journeys.

References

1. J. Li, Z. Skeete, S. Shan, S. Yan, K. Kurzatkowska, W. Zhao, Q.M. Ngo, P. Holubovska, J. Luo, M. Hepe, C. Zhong, “Surface Enhanced Raman Scattering Detection of Cancer Biomarkers with Bifunctional Nanocomposite Probes,” Anal. Chem, 87, 10698-10702 (2015).

2. M. Vendrell, K.K. Maiti, K. Dhaliwal, Y. Chang, “Surface-enhanced Raman scattering in cancer detection and imaging,” Trends in Biotechnology. 31. 4, 249-257 (2013).

3. L. Fabris, “SERS Tags: The Next Promising Tool for Personalized Cancer Detection?” Chemnanomat. 2. 4, 249-258 (2016).

4. M.D. Sonntag, J.M. Klingsporn, A.B. Zrimsek, B. Sharma, L.K. Ruvuna, R.P. Van Duyne, “Molecular plasmonics for nanoscale spectroscopy,” Chem. Soc. Rev. 4 (2014).

5. K.T. Crampton, A. Zeytunyan, A.S. Fast, F.T. Ladani, A. Alfonso-Garcia, M. Banik, S. Yampolsky, D.A. Fishman, E.O. Potma, V.A. Apkarian, “Ultrafast Coherent Raman Scattering at Plasmonic Nanojunctions,” J. Phys. Chem. C. 120 (37), 20943-20953 (2016).

6. S. Yampolsky, D.A. Fishman, S. Dey, E. Hulkko, M. Banik, E.O. Potma, V.A. Apkarian, “Seeing a single molecule vibrate through time-resolved coherent anti-Stokes Raman scattering,” Nature Photonics. 8, 650-656 (2014).

7. A.D. McFarland, C.L. Haynes, C.A. Mirkin, R.P. Van Duyne, H.A. Godwin, “Color My Nanoworld,” J. Chem. Educ. 81 (4), 544A (2004).

8. I.E. Pavel, K.S. Alnajjar, J.L. Monahan, A. Stahler, N.E. Hunter, K.M Weaver, J.D. Baker, A.J. Meyerhoefer, D.A. Dolson, “Estimating the Analytical and Surface Enhancement

Factors in Surface-Enhanced Raman Scattering (SERS): A Novel Physical Chemistry and Nanotechnology Laboratory Experiment," J. Chem. Educ. 89 (2), 286-290 (2012).

9. J. Masson, H. Yockell-Leilievre, "Spectroscopic and Physical Characteriation of Functionalized Au Nanoparticles: A Multiweek Experimental Project," J. Chem. Educ. 91 (10), 1557-1562 (2014).

10. C.S. Schnitzer, C.L. Reim, J.J. Sirois, "Surface-Enhanced Resonance Raman Scattering and Visible Extinction Spectroscopy of Copper Chlorophyllin: An Upper Level Chemistry Experiment," J. Chem. Educ. 87 (4), 429-432 (2010).

11. B. Albee, K.D. Edwards, E.O. Potma, "Simply SERS: Experiment for General Chemistry Laboratory," J. Chem. Educ. In Submission (2017).

12. K. Cottingham, "SERS enters the art scene," Anal. Chem. 81 (17), 7128-7128 (2009).

13. F. Pozzi, M. Leona, "Surface-enhanced Raman spectroscopy in art and archaelogy," J. Raman Spectrosc. 47 (1), 67-77 (2015).

14. J.Y Roh, M.K. Matecki, S.A. Svoboda, K.L. Wustholz, "Identifying Pigment Mixtures in Art Using SERS: A Treatment Flowchart Approach," Anal. Chem. 88 (4), 2028-2032 (2016).

15. T. Li, B. Albee, M. Alemayehu, R. Diaz, L. Ingham, S. Kamal, M. Rodriguez, S.W. Bishnoi, "Comparative toxicity study of Ag, Au, and Ag-Au bimetallic nanoparticles on Daphnia Magna," Anal. Bioanal. Chem. 398 (2), 689-700 (2010).

CHAPTER 3: Remote SPP Driven Electron Tunneling in nm-sized Au Nanojunctions

3.1 Background and Significance

Now that we have introduced plasmonics in Au nanomaterials through the development of a teaching lab based on the concepts of SERS in Chapter 2, we will now shift our focus to a different application of plasmonic Au nanostructures: Using Surface Plasmon Polaritons (SPPs) as a means of driving nanocircuits.

SPPs are propagating waves of oscillating electromagnetic energy, which are directed along the surface of a thin-film of metal, such as gold, through plasmonic coupling. The coupling of electromagnetic energy efficiency to these modes has interesting implications in the conversion of light to energy. Furthermore, the fact that SPP modes can be remotely controlled and guided to a precise location implies that SPP modes can be used not only to convert light to energy, but also to use that energy to power nanocircuits which may be of use in nanoscale computing applications among other fields.

To better understand this potential, this chapter seeks to explore the physical properties of metal-insulator-metal (MIM) tunneling junctions when excited by ultrafast SPPs remotely. We will present a series of studies that focus on electron transport in 4-20nm MIM nanojunctions constructed in 20nm Au thin-films. Such junctions can be reproducibly fabricated using a combination of focused ion beam milling (FIB) and electromigration (EM) techniques. Furthermore, these devices are excited and analyzed under ambient conditions.

Using these methods, we demonstrate the generation of tunneling current, observing a transition between Tien-Gordon type tunneling at lower fields, into Fowler-Nordheim type field emission in higher field regimes. In larger gaps, the dominant mechanism of electron transport is observed to be Fowler-Nordheim type field emission.

The goal of this chapter is to explore the details about how this process works at a fundamental physical level experimentally. We will also highlight how this process can be further improved using atomic layer deposition (ALD) coated alumina nanofilms, and applied to molecular junctions that allow for studies of electron transport though single molecule nanocircuits using DNA linked nanocubes. Finally, we will examine the theoretical prediction of this phenomenon, and how well the theory fits observations made during studies. Controlling and understanding such phenomenon allows for a newer, even smaller alternative in the design of devices used for light-to-energy conversion.

3.1.1 Electron Transport Mechanics

In the absence of light, electrons can tunnel across sub nm MIM junctions. This transport is generally modeled by the Wentzel-Kramers-Brillouin (WKB) electron transport model, developed in 1926 and named after its founders.

When light is applied to such gaps, an electric field oscillation occurs in the MIM nanojunction. This oscillation, in turn, produces a potential energy difference between the metal electrodes separated by an insulating layer such as air. The application of a static dc bias across a MIM nanojunctions results in an offset in the Fermi levels of each electrode, to produce an asymmetry in the electron density on each side of the energy barrier. The

application of light to this junction adds an additional oscillating ac electric field element into the system, causing the electron density on each side of the barrier to fluctuate. From a classical perspective, this process results in a measureable dc current, in a process known as optical rectification [1]. This process may also be described quantum-mechanically by the models of Tien and Gordon, which examine changes in the electron density of states because of an optical modulation of the energy barrier [2,3]. This concept is detailed in Figure 3.1, showing the bending of a potential energy barrier as a function of applied field.

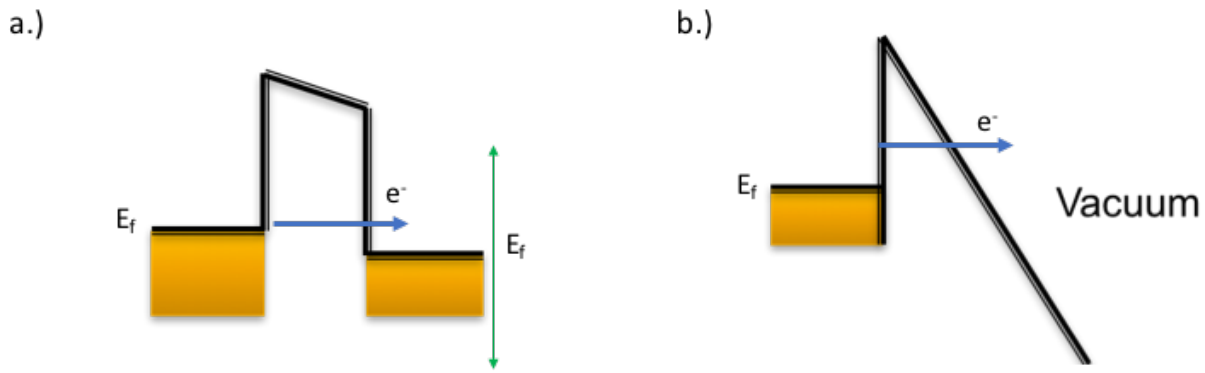

Figure 3.1: The bending of a potential energy barrier as a function of applied field. In the case of a.) Tien-Gordon AC Tunneling, AC modulation of the barrier yields tunneling due to a fluctuation in the electron density in the electrodes separated by the barrier indicated by the green arrow. The direction of tunneling current is influenced by applying a static dc bias to produce a net barrier asymmetry during modulation. In the case of b.) Fowler-Nordheim Field Emission, a high field bends the barrier sufficiently to induce tunneling into vacuum, resulting in field emission from electrons escaping the thinned barrier in the heavily modulated junction.

3.1.2 Tunneling Direction and Field Emission

The direction of tunneling in nm-scale MIM junctions is generally a function of gap symmetry. As previously stated, electron tunneling can occur through a potential energy barrier in the absence of light. If a very high electric field is applied to such a junction, the energy barrier is bent drastically compared to cases in which a relatively low optical field is applied, shorting tunneling distance in the energy barrier. This process facilitates electrons tunneling across the junction, giving rise to Fowler-Nordheim field emission in the direction favored by the Fermi level asymmetry between the two electrodes [3,4]. The direction of tunneling induced by optically relevant processes including SPPs can be controlled and manipulated using an external bias.

3.1.3 Optical Rectification

Interestingly, the earliest examples of optical rectification devices come from the scanning tunneling microscopy (STM) community, soon followed by similar observations in 2d nanocircuit break junctions and molecular junctions [5-9]. In these studies, it is significant to note that the behavior of the tunneling current in these studies is also consistent with the Tien-Gordon model for ac tunneling through a modulated energy barrier. For high gap fields, it has been demonstrated that field emission is the dominant physical mechanism for electron transport across a MIM junction [10].

Despite this knowledge, there are still many things that are not clear about the physical characteristics of optical rectenna, which have historically been studied under conditions of direct optical illumination. For example, it has been suggested that gap-size dependent charge-transfer plasmons play a role in the process of optical rectification [11]. In addition, the

inclusion of a quantum mechanical descriptions dealing with the role conduction electrons play in a tunneling barrier during optical rectification has been debated in other studies [12]. A major reason for this gap in knowledge is the difficulty in producing devices small enough to study, as well as fighting rapid thermal degradation of these structures while being measured under illumination. This chapter will later demonstrate the use of focused ion beam milling and electromigration as a means of producing stable nm-sized tunneling junctions, as well as using alumina to thermally stabilize MIM nanojunctions.

3.1.4 Surface Plasmon Polaritons

When directly illuminated, the high fields generated in the gap induce rapid heating at the nanoscale. The heat confined in the gap causes structural damage, as atoms migrate and gaps become too large for direct measurements of tunneling current. As a result, a remote excitation mechanism can be used to generate electron tunneling events that induces less heat and allows for better stability of tunneling junctions. To do this, we use remotely launched SPP modes to drive electron tunneling in Au-Air-Au nanojunctions. The remote launching of SPPs in Au thin-films is detailed in Figure 3.2.

To drive the devices, which we will describe later in this chapter, it is also key to understand the basic physical properties of SPPs. Early examples of SPP experiments demonstrating these basic properties include the remote imaging of a single Si nanoparticle with Coherent Anti-Stokes Spectroscopy (CARS) using SPPs [13]. There are also interesting examples showing the use of SPPs to induce electron tunneling in a silver tip, having direct implications for plasmon driven Scanning Tunneling Microscopy [10, 14]. Additionally, these

plasmon modes have a direct connection to another interesting device that has been studied throughout the literature, the optical rectenna, which we will also discuss in greater detail later in this chapter.

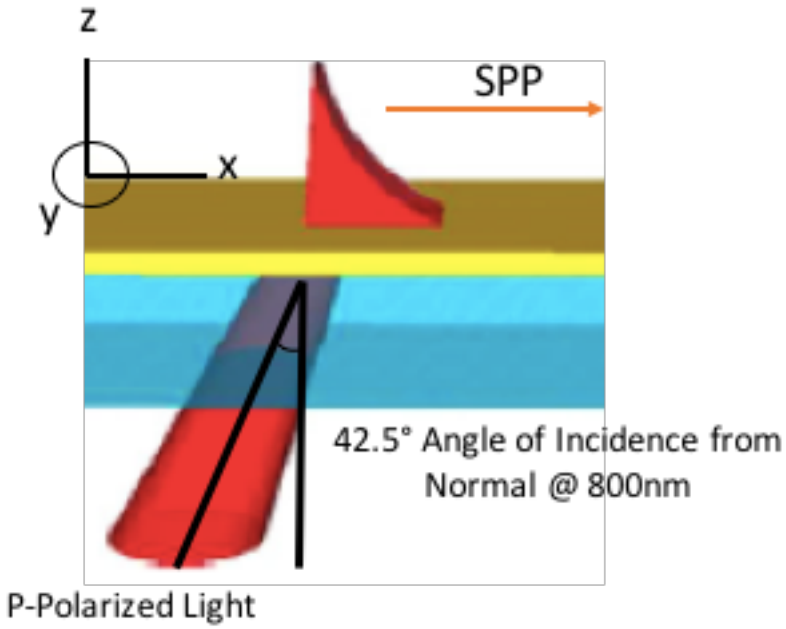

Figure 3.2: The propagation of an SPP mode in at a gold, air interface using a-Kretschmann type configuration. As demonstrated in the schematic, experiments in this chapter will focus on propagation of such SPP modes at a wavelength of 800nm. To launch an SPP in such a configuration at this wavelength, an angle of incidence 42.5° from normal must be used to illuminate the device and couple light into a propagating SPP mode. In addition, the light must be p-polarized. This ensures a z-component to the input electric field, which can couple into the film, driving an SPP mode along the surface.

To launch an SPP with the efficiency required to perform this type of excitation requires the realization of many parameters including and not limited to thin-film material choice, wavelength (frequency) of light used, angle of incoming light beam, and finally polarization. The ideal choice of material to use for the launching of SPP modes along a thin-film surface is a plasmonically active material, such as gold, silver, copper, platinum, and aluminum. This is because of the collective oscillation in surface electrons in optically relevant wavelengths in these materials [15-18]. In the studies described in this chapter, the choice of thin-film is gold due to its stability and low oxidation rate. To launch an SPP mode along the surface of such a thin-film, an angle of incidence of 42.5° must be achieved using a Kretechmann type configuration, where the SPP is excited through a glass-gold interface, and propagated along the gold-air interface on the other side [13]. In addition, the polarization of the excitation beam must be set to allow p-polarized light to interact with the thin-film such that an SPP is launched along the surface. This is because of the relevant non-zero electric field components of p-polarized light with respect to the z-axis component allowing for coupling of the light into a propagating SPP. In s-polarization on the other hand, there is a lack of z-axis contribution with respect to the electric field interacting with the surface of the gold film. As a result, SPPs are not excited when using s-polarized light.

3.2 Understanding Field Strengths in Gaps using COMSOL Simulations

To simulate the experiment in a way to meaningfully understand the enhancement of the field in the nanogaps fabricated, a COMSOL simulation was performed to simulate the propagation of the SPP wave along the surface of a three-dimensional, Au nanojunction with a

geometry as used in experiments. The results of this simulation are summarized in Figure 3.3 and were performed with the collaborative help of Faezeh Tork Ladani [19]. As is demonstrated, in the case of a gap ranging from 4-10 nm, a very strong enhancement is expected at the site of the engineered nanogap. The strength of this field is expected to be strong enough to induce electron tunneling due to its estimated enhancement factor of 16. In the experiments that will be described in this chapter, it was determined that a field enhancement factor of 10 is more realistic. Regardless, we will demonstrate experimentally that the results are in line with the expected field confinement and enhancement that allows for SPP driven electron tunneling.

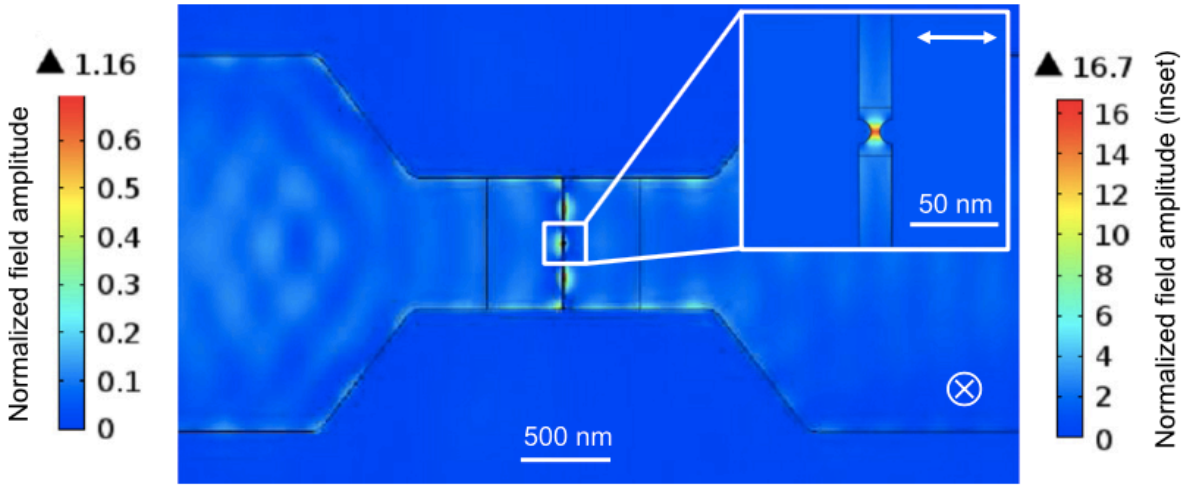

Figure 3.3: COMSOL FEM simulation of propagating SPP waves in the vicinity of a nanojunction, using an excitation wavelength of 800 nm and a film thickness of 30nm. The scale bar on the left shows the magnitude of the field in normalized units relative to the magnitude of the incident light field. The SPP propagation in the simulation moves from left to right in the above image with the out of plane electric field component being shown. The inset in the upper right corner shows a zoomed in region of simulated nanogap, where the electric field component polarized longitudinally in the gap is highly concentrated. The scale bar to the right shows the magnitude of the field depicted in the inset, normalized to the amplitude of the incident field. In this simulation, the effective electric field enhancement factor in the nanogap during excitation by an 800nm SPP is ~16. Image courtesy of Faezeh Tork Ladani, reproduced by permission from IOP Publishing [19].

3.3 Electron Tunneling Driven by Ultrafast SPP Modes

Now that we have discussed the basic physical properties that are key to launch an SPP mode along the surface of an Au thin-film, we will focus on the experimental details that allow for the generation of remote controlled, ultrafast electron transport in MIM nanojunctions. To perform this set of experiments, a few key parameters will be highlighted, including and not limited to, the construction of MIM nanojunctions used in these studies, the SPP launching geometry, polarization dependence of the SPP driven tunneling current, gap-size dependence, and structural stability.

3.3.1 Thermal Deposition of Au Thin Films

To begin this experiment, a suitable MIM nanojunction must be constructed that allows for the launching of an SPP mode that can be monitored electrically, while simultaneously being excited optically. To fully understand the range of physical parameters that is important for the generation of tunneling current induced by an SPP mode, it is key to ensure that devices with a good range of gap sizes are examined. In this set of experiments, a gap range of 4-20nm was targeted to understand the limits of tunneling driven by SPPs over a wide range of gap sizes. To achieve gaps ranging from 4-20nm, four key techniques were used for the construction of our devices: Thermal Deposition of template Au thin-films, Photolithography production of Au micro-bowties as a template for nanoscale MIM junctions, and finally a combination of Focused Ion Beam (FIB) milling and electromigration to produce the final MIM excited by SPPs in these studies.

To produce the template that our device is constructed from, a 20nm thin-film of Au is first deposited onto clean thin cover glass slips (Fisher, 22x22mm). The glass is cleaned by first sonicating the cover slips in acetone for 20minutes, followed by sonication in ethanol and nanopure water for 20 minutes each as well to remove any organic impurities and dust from the surface prior to the deposition of Au that would cause adhesion issues during deposition. The samples were also plasma cleaned for 2 minutes after solvent cleaning to ensure a well hydroxylated glass surface for optimal adhesion of the Au thin film to the glass cover slips. Once the thin cover slips were precleaned, the Au thin films were deposited using a Denton Vacuum high vacuum thermal deposition system. This system is capable of measuring thickness of deposited films to an angstrom level, allowing for the precise preparation of Au thin-films at a thickness of 20nm. This thickness was primarily chosen to aid in subsequent FIB milling fabrication steps that will be discussed shortly.

3.3.2 Focused Ion Beam Milling of Au Nanojunction Templates

The next step of construction, with respect to our nanojunctions was to prepare a template of gold bowties with bias contacts. This was achieved with photolithography using the thermally deposited 20nm Au thin films from the first steps of fabrication. To perform this step of the fabrication procedure, a positive photoresist (MicroChem, S1808) was coated onto the surface of clean thin-cover glass using a commercial spin coater for 90 seconds at a spin rate of 1700RPM. After coating, the films were hardened at 90°C for 30 min, and cooled to room temperature. A custom photomask was used to block the geometry of the desired bowtie templates during exposure to UV light. After exposure, the slides were developed in

MF-319 commercial developer and etched in a commercial KI: I_2: H2O complex to remove the unwanted gold, leaving behind a series of six bowties with bias contact pads that can be further processed to yield MIM nanojunctions used in our studies.

Once the micro-bowtie templates are ready using photolithography, the next step in the fabrication process involves using a combination focused ion beam milling and electromigration techniques to slim down the micro-bowties to form nanoscale MIM junctions. This is performed using an FEI Quanta 3d SEM/FIB. First, the nanowire in the bowtie template produced during photolithography steps is slimmed down from its native 2 um width to only 500nm. For gaps that are larger than 10nm, a gash can be cut fully through the wire to produce a gap suitable for SPP excitement directly. Unfortunately, since the resolution limit for milling with this microscope is around 10nm, it is not possible to produce the smaller gaps required to complete this set of studies. The next section of this chapter will detail further processing that can be performed to produce consistent gaps in this range. This process is detailed in its entirety in Figure 3.4.

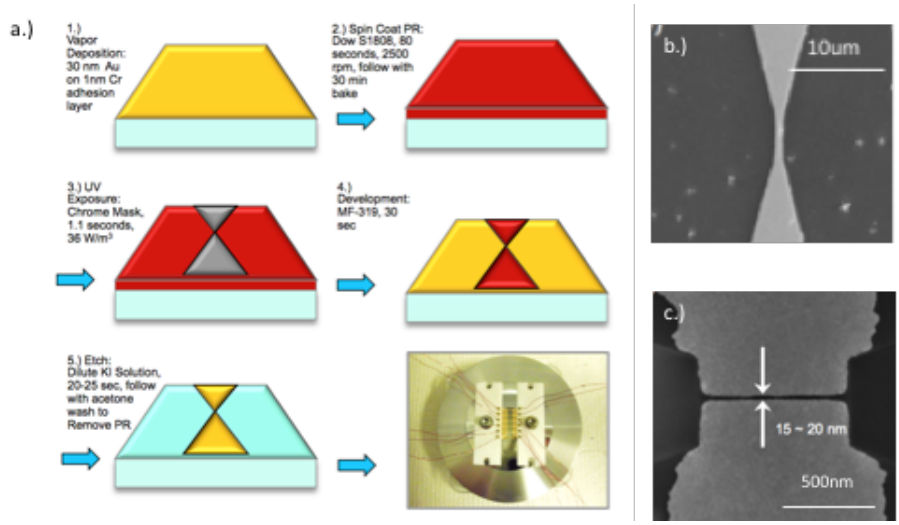

Figure 3.4: a.) Fabrication process of Au Nanogaps for remote generation of SPP induced electron tunneling events. As demonstrated a combination of photolithography and focused ion beam milling processes can be used in conjunction to produce the b,) bowtie templates and c.) required gaps ranging from 10-20nm needed for experiments.

3.3.3 Electromigration for Fabrication of sub-10nm Nanogaps in Au Bowties

To produce gaps that are sub 10-nm in size, we must employ one extra step to the fabrication process, electromigration. To perform this step, we adapt an experimental technique from Xiang et. al., used to produce reconnectable nm-scale gaps in gold and silver nanowires [20]. To induce electromigration in our bowties, a LabVIEW controlled Keithley 2400 source meter was used to ramp a voltage in the bowtie while monitoring the resistance in the device. As the voltage is ramped up, the increasing current bottleneck in the bowtie causes resistive heating to build up in the thinnest part of the nanowire in the bowtie template. This increase in heat in turn causes a migration of atoms in the wire at the weakest point of contact. As the atoms disconnect and form a gap, the resistance of the junction also increases. To facilitate the location and size of an electromigrated gap, a slight cut can be introduced into the nanowire prior to electromigration using FIB milling, like the direct construction of gaps 10nm and larger. If the proper cutoff resistance is set in the LabVIEW controlled voltage sweep for these partially milled wire templates, in this case 1kOhm, a gap ranging from 4-6nm can be reproducibly achieved. Though this combination of fabrication techniques, we can controllably produce tunneling junctions in Au-Air-Au nanojunctions from 4-20nm. An example of such a junction is depicted in figure 3.5.

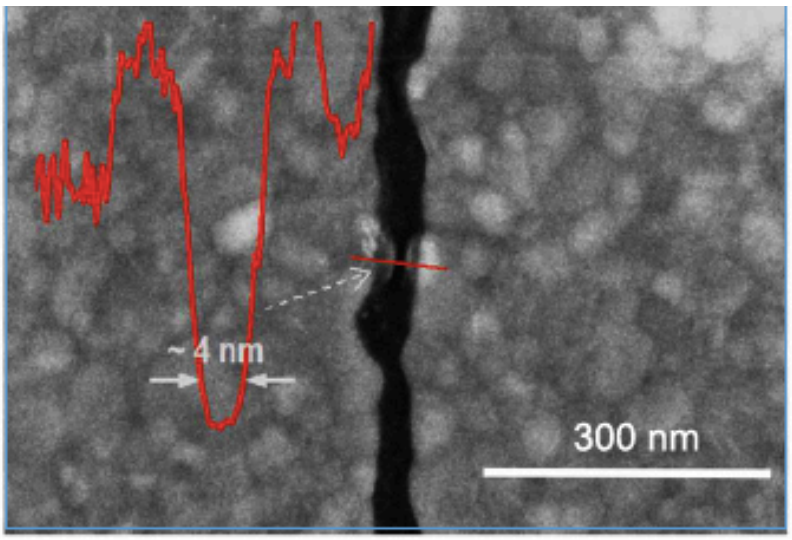

Figure 3.5: A 4nm junction prepared in a bowtie junction using a combination of FIB milling and electromigration.

Image reproduced by permission of IOP Publishing [19].

3.3.4 Generation of Tunneling Current through the Remote Launching of an SPP

To launch an SPP mode and measure the dc tunneling current generated by the remote excitation of the MIM nanojunctions constructed in this set of experiments, a custom ultrafast inverted optical microscope was constructed to simultaneously introduce an SPP mode into a 20 Au thin film bowtie junction while also measuring the tunneling current along the surface of the film. A detailed schematic of this excitation is given in Figure 3.6.

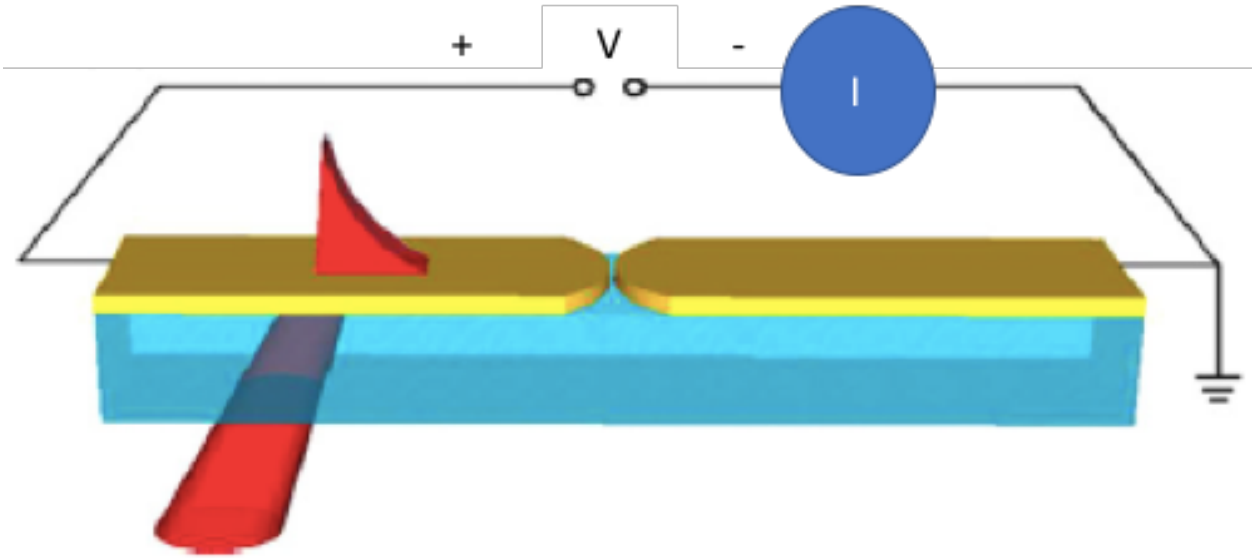

Figure 3.6: Schematic of the measurement of photo-induced tunneling current driven by remotely launched SPP modes using a Kretschmann type configuration. The laser beam is incident to the film at an angle of 42.5° through the glass to launch an SPP mode 10um away from the nanogap along the gold air interface [19].

To introduce a static dc bias to produce a Fermi level asymmetry between the electrodes of the junction and simultaneously measure tunneling current generated during SPP excitation, a custom microscope stage adapter was built that allowed for the electrical isolation and measurement of generated tunneling current for each bowtie nanojunction while being illuminated. This custom adapter is also detailed in Figure 3.4, holding a bowtie fabricated through our chemical processing methods. A bias was introduced to the sample using a Keithley 2400 sourcemeter. The current output of the circuit during SPP excitation was connected to a Stanford Research Systems voltage preamplifier, and measured through a home built LabVIEW program, that also performed a laser power sweep during the measurement of current.

To introduce the SPP into the thin-film, a Kretschmann type configuration was constructed using our inverted microscope (Olympus IX71) to couple a SPP into the fabricated Au nanojunctions. The laser source used to excite the SPP was a Coherent Mira 900 (800nm, 150fs) ultrafast Ti:Saph laser. A high N.A. microscope objective (Olympus, 60X, 1.42 N.A., Oil immersion) was used to ensure a wide enough optical collection angle to both excite, and image the launching of an SPP mode in the devices. To launch an SPP mode in Au, an angle of incidence of 42.5° and p-polarization is required to match the momentum conditions needed for surface field propagation. The polarization is controlled using a half-wave plate prior to the coupling of the ultrafast laser source to the inverted microscope. Images of the propagation of the SPPs in our nanojunctions was recorded using an Andor CDD camera connected to the output of the inverted microscope. An example of an SPP mode being propagated and confined to a nanojunction is demonstrated in figure 3.7.

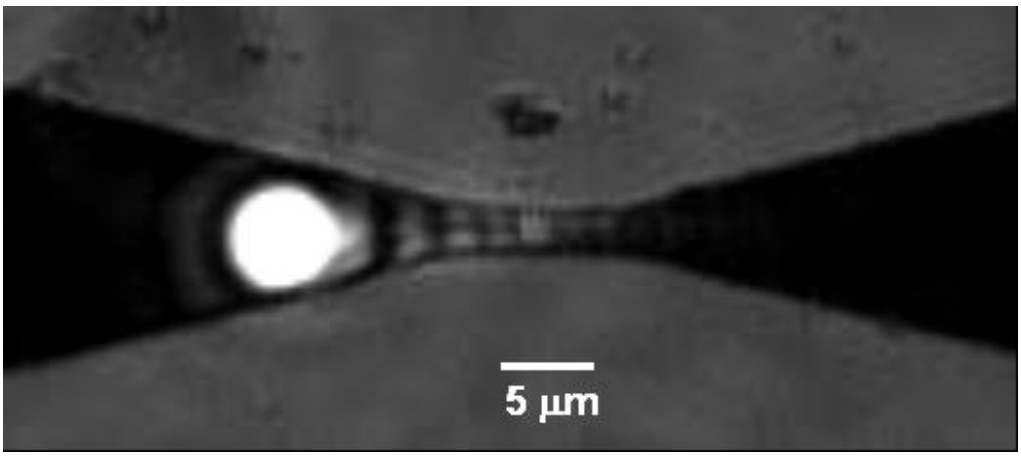

Figure 3.7: Demonstration of the launching of an SPP mode into a nanogap. As shown, the SPP is launched into the junction from approximately 10um away from the gap. The field is tightly focused to the gap as it propagates along the surface of the gold bowtie template, where it is enhanced by the gap, allowing for electron tunneling event to occur. This process will be detailed later in the chapter when simulations are further explored [19].

3.3.5 Polarization Dependence

To ensure that the generation of observed tunneling current was caused by remotely launched SPP modes, a polarization dependence study was performed at a constant optical power. Polarization of the incoming excitation was controlled using a half-wave plate prior to introduction of the beam to the Au nanojunction surface. The tunneling current of the device was measured using a Keithley 2400 source meter and recorded as the polarization was changed. To facilitate electron transfer, a static bias of .1V was also introduced into the system to ensure an offset in Fermi levels with respect to the two electrodes. The results of this measurement are detailed in Figure 3.8. As we can see, the tunneling current of the device is most significant in the p-polarization state, and goes to zero in the s-polarization state as the waveplate is rotated throughout the measurement.

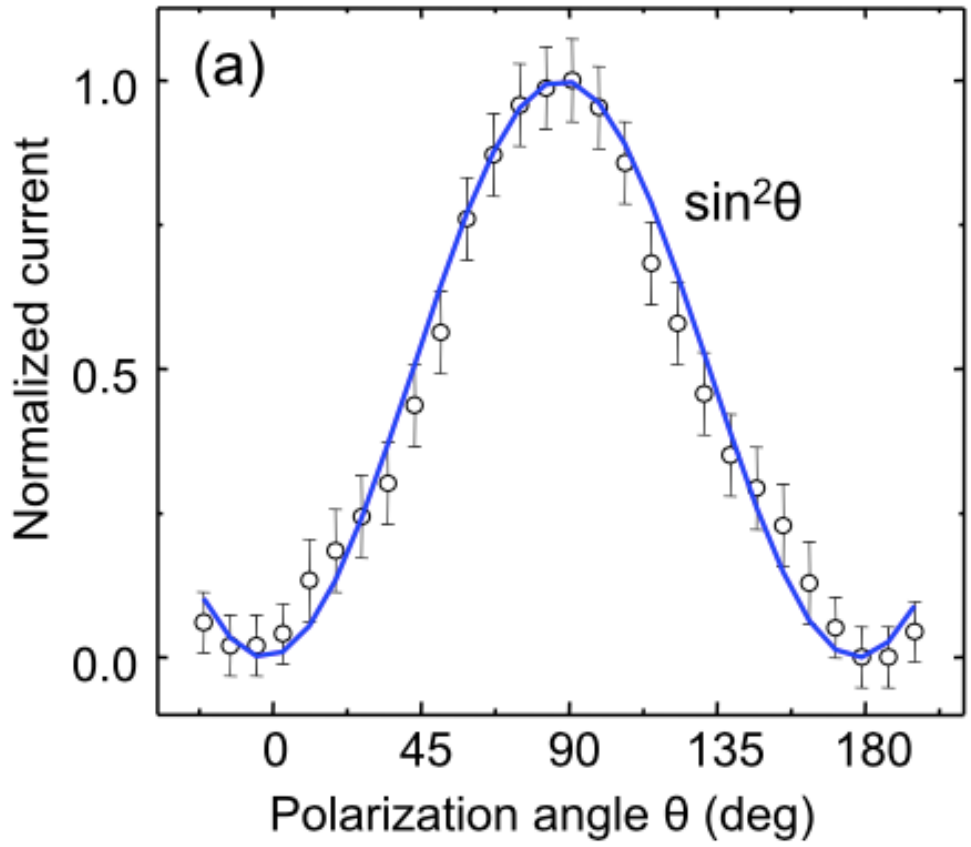

Figure 3.8: Polarization dependence of induced tunneling current under an incident laser power density of 24 kW cm−2 (800 nm) during the launching of an SPP mode. A bias of +0.2 V has also been introduced into the system using a Keithley 2400 Sourcemeter. The current is normalized to the highest value in the measurement in this plot. The trend demonstrates that tunneling current is only generated in the p-polarization state (90°) and goes to zero at 0° and 180° respectively (s-polarization). This confirms that the measured tunneling current is indeed generated by the launching of a remote SPP mode into the tunneling junction. Image reproduced by permission of IOP Publishing [19].

3.3.6 Gap-Size Dependence

To understand the role gap-size dependent process such as charge transfer plasmons or Tien-Gordon type tunneling play in electron transport in nanogaps a range of devices were measured using a home built LabVIEW program that performed an automated laser power sweep, while simultaneously measuring the tunneling current of the device being monitored by way of a SRS voltage preamplifier, connected to the Keithley 2400 sourcemeter. This sourcemeter was also used to introduce a static dc bias of .1V to offset the Fermi levels of the electrodes prior to introduction of the SPP mode into the system. The range of gaps monitored using this setup was 4-12nm.

The results of this set of experiments is detailed in figure 3.9. As demonstrated, for gaps 5nm or smaller, a linear tunneling current can be seen in the low field regime during the power sweep that transitions into a more exponential trend in the high field regime. For gaps, greater than 5nm wide, this linear low field trend is not visible in measurements of the tunneling current. At high fields though, like in smaller gaps, an exponential character is seen in the measured tunneling current. The linear tunneling current behavior seen in sub-5nm gaps is in line with the observations and theory of Tien-Gordon AC Tunneling. We will explore the physical reasons for this observation later, as we delve into simulations performed to confirm these experimental results. The exponential high-field region follows a trend that is more in line with the observations and theory of Fowler-Nordheim field emission. The transition of tunneling current from a low field linear regime to a high-field exponential regime in the smaller devices suggests a coupling and strong enhancement of the SPP in the nanojunction that facilitates electron transfer between the electrodes that is not present in larger gaps. For

these larger gaps, the barrier must be sufficiently thinned enough through bending to allow for efficient transfer of the electrons from one side of the nanogap to the other. These claims will also be further examined in later sections of this chapter detailing theoretical studies performed in these nanojunctions.

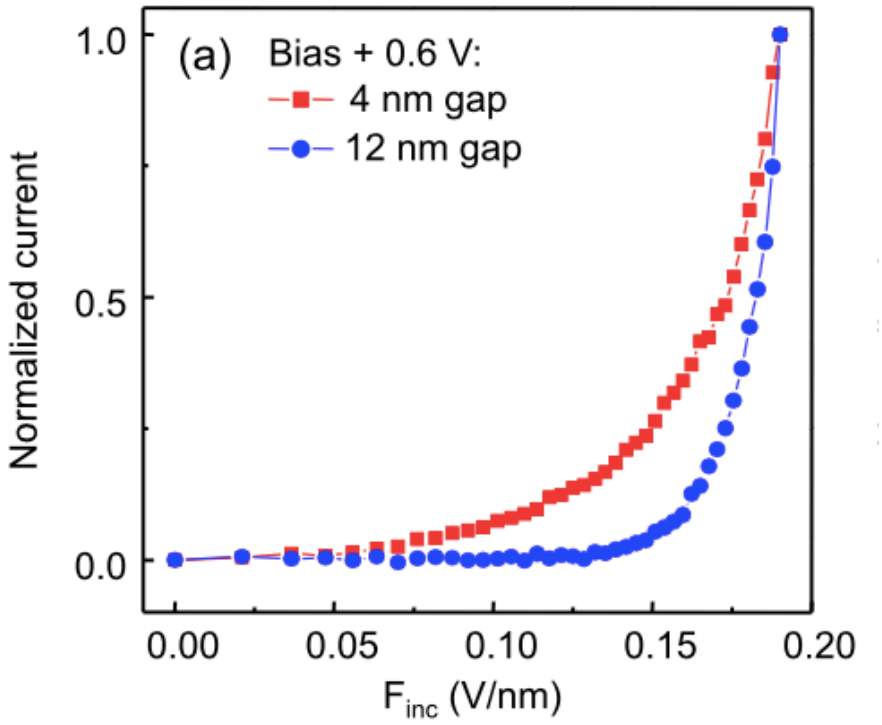

Figure 3.9: Tunneling current as a function of field for a 4 and 12 nm gap. The current is normalized for the highest value of the experimental measurement with a static .6V bias being introduced into the system during measurements. As demonstrated in sub-5nm gaps, a inear low field tunneling current can be seen that transitions into a dominantly exponential high field regime. For the 12nm gap, only a high field exponential type field emission can be measured. Image reproduced by permission of IOP Publishing [19].

3.3.7 Structure Heating from SPP and Tunneling Current Stability

Unfortunately, it was discovered that the thermal stability of the devices measured under ambient conditions is relatively low due to the buildup of heat in the fabricated nanojunctions during SPP excitation. For small gaps, less than 5nm, the linear low field tunneling current could only be measured a few times before thermal damage caused the gap to grow to sizes too large to see this physical tunneling regime in measurements. The thermal stability of larger gaps was slightly better, but also subject to thermal damage and uncontrolled gap growth during SPP excitation of the nanogap. As demonstrated in Figure 3.10, when a change in morphology occurs during a measurement, a sharp change in the tunneling current from the expected linear or exponential trends is obvious. Current increases when gap size is shortened by thermal migration of Au atoms in the nanogap, and decreases when the gap is increased in size. This process is like the resistive heating that is used to perform electromigration in the initial construction of the nanogaps in fabrication and tends to favor gap size growth, rather than shrinkage in observations during experiments. We will discuss ways to minimize these effects next.

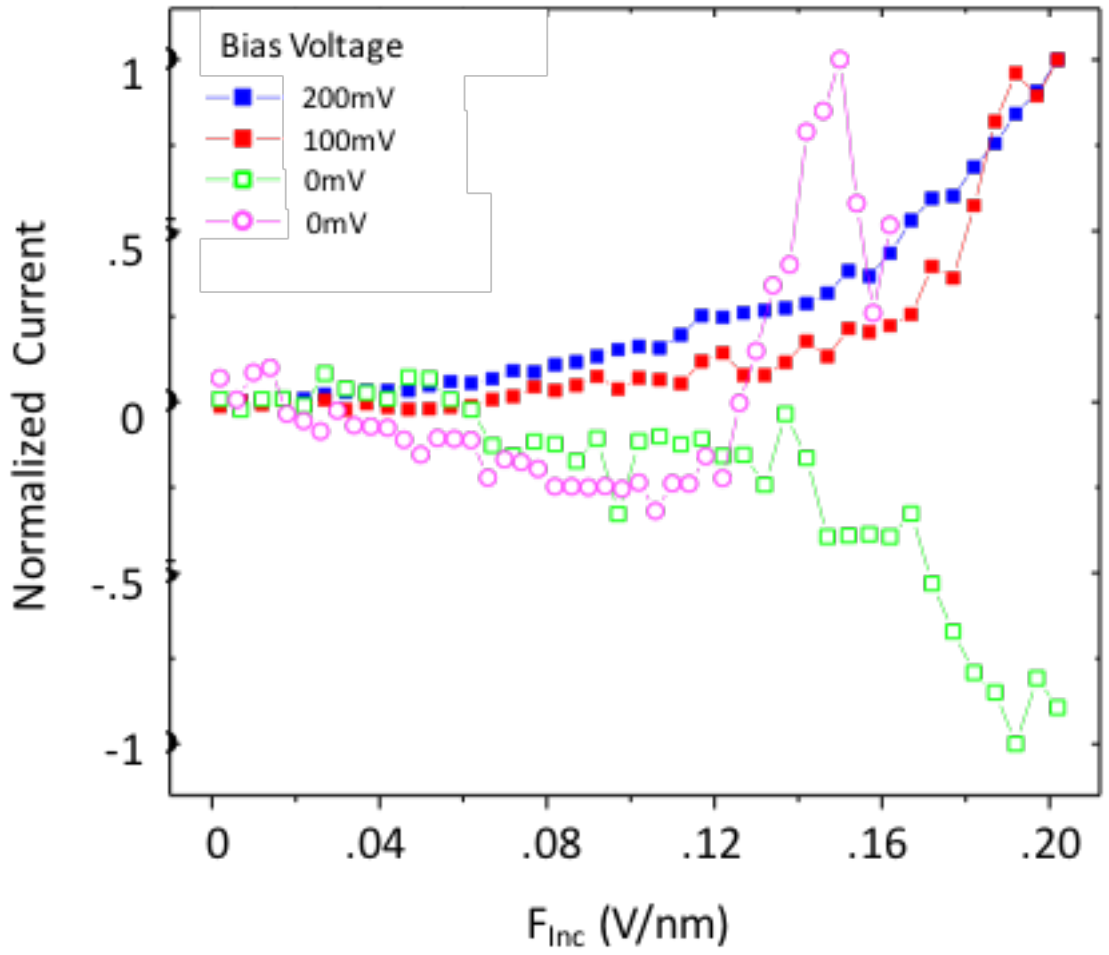

Figure 3.10: Fluctuations in the tunneling current during measurements can be seen through changes in the tunneling currents from the expected linear and exponential fit as a function of field. Though structural changes may be induced through thermal effects induced by the SPP at the nanojunction at low fields, greater effects are generally apparent in the observed tunneling current in the high field regime.

3.4 Improving Stability of Devices Using Alumina

It is very common for MIM optical rectennas to change morphology due to heating effects while under illumination from Angstroms to nm rapidly. This quickly reduces the measurable photo current achievable in such devices, limiting their ultimate use in the commercial applications of tomorrow. Here we will discuss the use of atomic layer deposition (ALD) to introduce alumina layers that aid in heat dissipation, and as a result significantly improve the performance lifetime of SPP driven tunneling junctions.

3.4.1 Basis for ALD of Alumina

It has been demonstrated in the literature [21] that the structural damage introduced to electric field nanoantennae by heat during illumination can be reduced by encapsulating dimers of gold and silver nanoparticles with silica in solution prior to spectroscopic measurement in single molecule, time-resolved CARS applications. This silica shell locks the structures in place while under illumination, providing a structural brace that fights changes in morphology in the illuminated particles as heat builds up in the system. As a result, the dimers can be measured significantly longer during single molecule spectroscopic studies before structural damage is too great for signals to be measured.

Alumina is believed to have very similar properties as silica with respect to its potential use as a structural support layer in similar plasmonic applications. Unlike silica, which is usually prepared through a sol-gel synthesis method, alumina may be deposited at very fine atomic scales using ALD. ALD uses a high vacuum system to thermally evaporate and oxidize

aluminum, layer by layer, until the desired thickness is achieved in the coating. This method allows for the deposition of films with precision levels down to the angstrom scale.

3.4.2 Improved Device Stability with Alumina

In this set of experiments, we used ALD to prepare a 70nm layer of alumina on top of our devices as a final fabrication add on step to the previously detailed procedures. This part of the work was performed in collaboration with the Law group at UCI. By working with the Law group to produce these thermal protection films, tunneling current could be measured in devices following the same physical trends as uncoated junctions in ambient conditions. A significant increase was seen in the number of times a device could be used before thermal damage had occurred to the point tunneling currents could not be measured during experiments.

3.5 Theoretical Validation of SPP Driven Electron Transport in nm-sized Junctions

To ensure that the physical observations detailed in this chapter from experiments are valid, it is crucial to compare the experimental results with the expected theory to verify the observed trends.

3.5.1 MathCAD Simulations

To better understand the physics demonstrated during electron tunneling driven by remote SPP modes, MathCAD simulations were performed using experimental parameters assuming a WKB approximation for the tunneling probability of an electron under the influence

of an ac and dc field. According to WKB theory the probability of an electron tunneling through a potential barrier can be expressed as:

$$D(E_z) = [\frac{-2\sqrt{2m}}{\hbar}\int_{z_1}^{z_2}\sqrt{V(z)-E_z}\ dz, \qquad (1)$$

where m is the mass of the electron, V(z) is the potential of the tunneling barrier, E_z is the energy of the electron involved in tunneling across the barrier.

When an extra dc bias is applied to this system, the tunneling current density is then formulated as:

$$J(V_b) = \int_0^{E_m} D(E_z)\zeta(E_z, V_b)dE_z, \qquad (2)$$

where Em is the maximum energy of the electrons involved in tunneling and $\zeta(E_z, V_b)$ is given by:

$$\zeta(E_z, V_b) = \frac{4\pi me}{h^3}\int_0^{\infty}[f_1(E_z + E_r) - f_2(E_z + E_r + eV_b)]dE_r, \qquad (3)$$

where f(E) is the Fermi-Dirac distribution function.

To simulate the tunneling current predicted by the experimental parameters achieved, equation 2 was used in MathCAD for 4 and 12nm nanojunctions. To match the experimental conditions used, a Fermi energy of 5.53eV was assumed, as well as a work function of 5.1 eV for the gold thin film. The photon energy of the laser used in the SPP driven excitation was assumed to be 1.55eV, with optical modulation of the barrier being considered. To obtain the

tunneling current, one integration is performed over a cycle of the driving field. The nonlinearity requirement for the system is modelled by simulating the field dependent modulation strength of the gap. As a result, the effective field in the gap for half of the optical cycle has a higher amplitude than the other half of the optical cycle. In this simulation, the potential barrier, V(z), is modeled with the image potential. We finally have assumed in these simulations that the electrons driven at energies $E_F + \hbar\omega$ are the primary contributors to electron tunneling. The results of these simulations are detailed in Figure 3.11.

As we show, the expected tunneling current is a function of applied bias, optical field magnitude, and the width of the gap. As was found in experiments, there are consistently different results in our simulations between the 4 and 12nm gap size cases. The trends in the expected tunneling currents using WKB theory match the experimentally determined cases for a 4 and 12nm SPP driven tunneling junction very well.

Furthermore, in the case of the 4nm gap, if we vary the function of V_b we see a quasi-linear trend in the low field limit in all cases, which changes to exponential field-emission type behavior in the high field limit. Although the tunneling current can be predicted, the WKB theory still is not able to discriminate the energy of the tunneling electrons directly. This is because relatively similar quantitative results are obtained in the simulations with electron tunneling energies of both E_F and $E_F + \hbar\omega$. It has been suggested in previous literature studies [22] that photo excited electrons which have dephased and lost their coherence are responsible for the dominant tunneling mechanism.

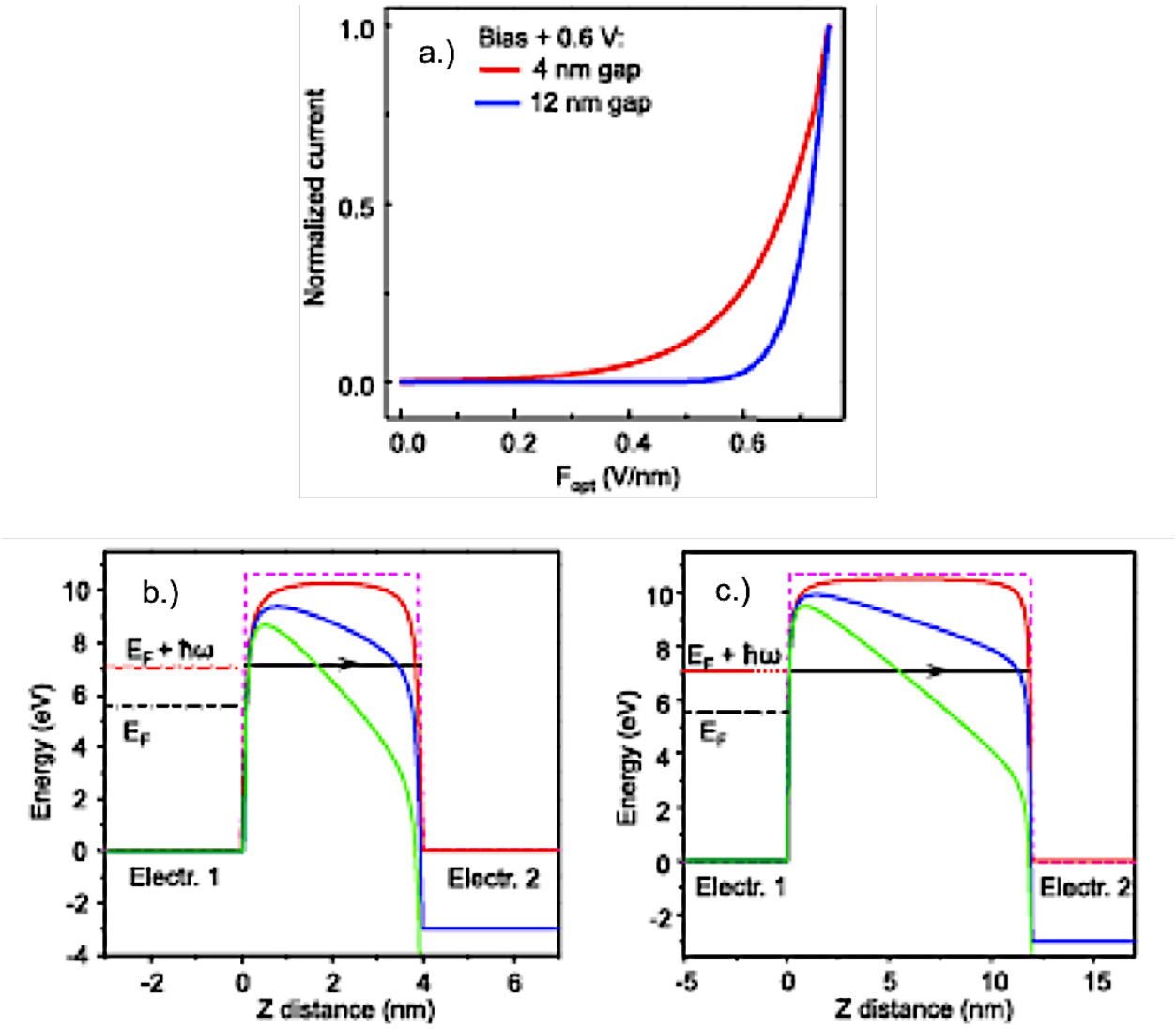

Figure 3.11: a.) Calculated tunneling current as a function of assumed local gap field intensity for two similar nanogaps including a rectangular and image potential barrier as a function of bias for the 4 and 12 nm nanogaps respectively. In both figures, the black dashed–dotted line and the red dotted line correspond to the Fermi energy and excited state assuming a 1.55eV excitation energy (EF + 1.55 eV). The biases included in simulations were 0 V (red), 3V (blue) and 7.5 V (green) [19].

3.6 Remote SPP Driven Two-Photon Electroluminesce (TPEL) in CdSe:ZnS Quantum Dots

By demonstrating that electron tunneling can be driven using SPPs, as well as through a variety of insulators, including and not limited to air and alumina a follow up experiment was performed to determine if tunneling could be used to power non-linear spectroscopic imaging processes in a remote manner.

To prepare a novel experiment demonstrating remotely driven TPEL using remote launched SPPs, a conducting film of PEDOT:PSS polymer (Sigma Aldrich, 2% in H_2O) was doped with CdSe:ZnS core-shell quantum dots (Sigma Aldrich, 1% by wt in Toluene) to produce a uM concentration of quantum dots in PEDOT:PSS. A total volume of 5uL was pipetted near a fabricated nanojunction to trap QDs on the surface of the gold film. Once pipetted in place, the sample was placed on a spin coater at 2900RPM for 1min, until the sample was dry. No post-baking procedures were performed in the films. The solution spun onto the gold samples contained 8 parts PEDOT: PSS solution to 2 parts QD solution as described above. The commercially produced QDs are reported to have an excitation wavelength of 645nm and an emission wavelength of 650nm.

Experimental results for this excitation are demonstrated in Figure 3.12. As shown, QDs trapped within the conductive polymer matrix are indeed lit up by the launching of remote SPP modes. The fact that the QDs emit at a known wavelength of 650nm implies that a process analogous to two-photon fluorescence is occurring in the fabricated devices. This demonstrates the potential use of SPP driven devices in next-generation commercial lighting applications and multi-photonic imaging in complex chemical systems driven with remotely

controlled excitation fields. Future work with respect to the improved construction and design of such devices may also prove to yield major advances multi-photonic imaging methods including, but not limited to Coherent Anti-Stokes Raman Spectroscopy, Second and Third Harmonic Generation, and Fluorescence Spectroscopy based imaging techniques.

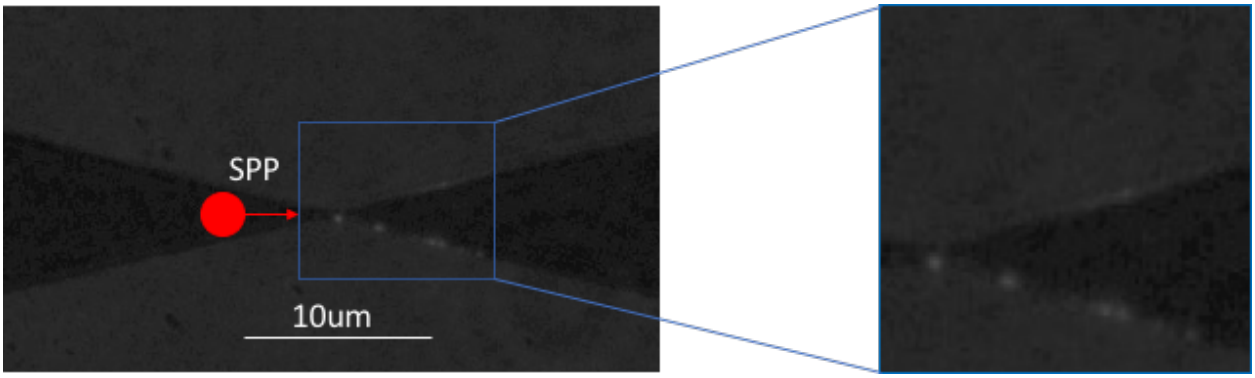

Figure 3.12: Two photon photo luminescence of CdSe:ZnS quantum dots lit up remotely using an ultrafast SPP mode, launched from a distance of about 10um from the emitting particles. The emission wavelength of the particles is 650nm.

3.7 Future Directions: Ultrafast DC Electronics Driven by SPPs

The driving of ultrafast dc current through electron transport in SPP junctions allows for a range of interesting applications in future research. Because the SPP mode launched in this study are excited using ultrafast lasers, the dc tunneling current generated in the experiments detailed above can be expected to be ultrafast. If this ultrafast dc current is directed through a molecular circuit, dc current can be used in future applications to induce and monitor electron dynamics in real time, simplifying electron transport studies significantly. This concept is detailed in Figure 3.13.

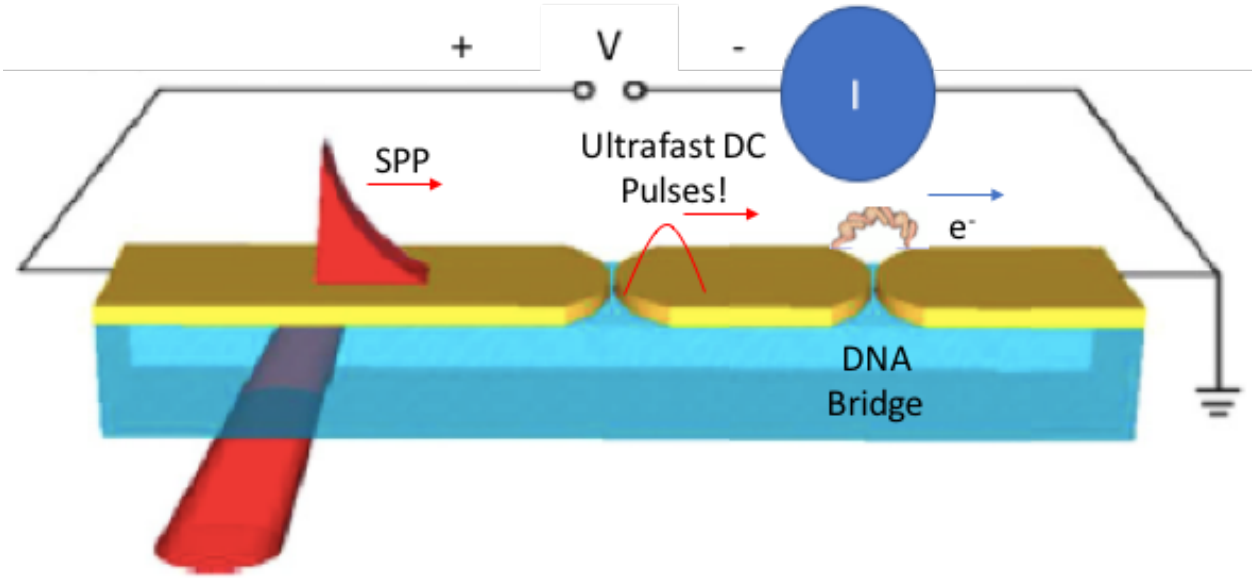

Figure 3.13: Schematic detailing the construction and generation of molecular circuits driven by ultrafast DC pulses generated by remote SPPs. Follow up studies using such platforms allows for ultrafast electron transport in single molecules in real-time as well as excitations of molecules using ultrafast DC current sources.

Such circuits can be easily constructed by adapting a procedure of Linkko et. al. [23], where a 1uM solution of DNA linked Ag nanocube dimers prepared by the Shumaker Perry Group at the University of Utah as part of the Chemistry at the Space Time Limit (CaSTL) Initiative was used to prepare a single DNA Linked dimer nanocircuit. To link the dimer to a fabricated nanojunction, a 5uL drop of the 1uM nanocube dimers was placed on top of the fabricated nanogap in a gold bowtie. Once this drop was placed, a function generator was used to introduce 5V of 10MHz ac current into the nanogap while measuring the resistance over the gap simultaneously. When the gap remained unconnected, a resistance in the MΩ range is expected. This very quickly drops to a measureable resistance in the kΩ range when a single dimer is attached. An SEM image of the results of this procedure can be seen in figure 3.14.

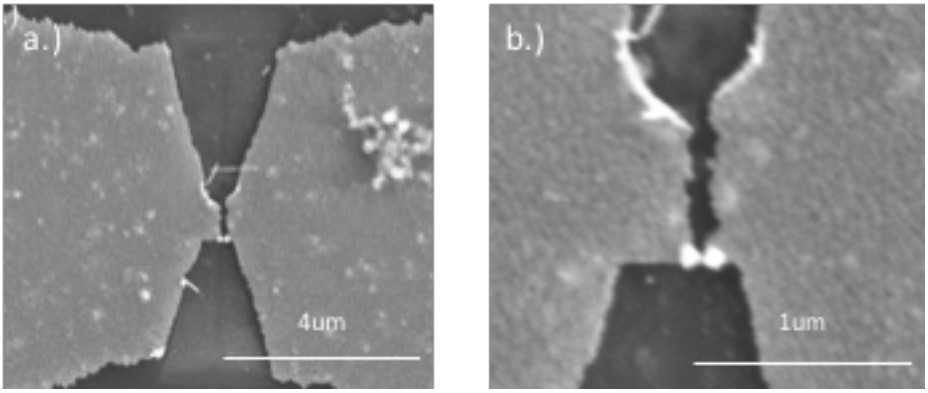

Figure 3.14: Single molecule DNA nanoelectronic device constructed using AC trapping of DNA-linked Ag Dimers. DNA-Linked Ag dimers were provided courtesy of the Shumaker-Parry Group at the University of Utah. To trap the dimer, a 5uL drop of 1uM Ag dimers dispersed in nanopure water was pipetted on top of a broken nanowire gap. 5V AC at a frequency of 100MHz was applied to the system for 5sec to trap the particle. SEM analysis performed after trapping of the dimer indicates the formation of a single dimer circuit that can be used to study electron transport dynamics in follow up studies.

Such circuits will be used in future studies using ultrafast dc pulses generated by remote SPPs to directly study electron transport dynamics in single molecule systems. If the nanogaps are arranged in the proper waveguide geometry, such single molecule electronics may quickly find a use in next generation, plasmonically activated integrated circuits.

3.8 Concluding Remarks

In this chapter, we have demonstrated the generation of SPP driven remote controlled electron tunneling in Au plasmonic nanojunctions. We have found a gap size dependence to a low field, quasi-linear tunneling current during excitation with SPPs in junctions <5nm in width, which transitions to an exponential power dependence at higher field regimes. The linear behavior is in line with observations described by Tien-Gordon ac tunneling, while the exponential behavior is more in line with Fowler-Norheim type field emission. In gaps, larger than 5nm, only a high field emission profile is seen in experiments in line with Fowler-Nordheim type field emission. Simulations performed using WKB approximations for the tunneling current generated by a remote launched SPP agree well with experimentally obtained results, and suggest that tunneling is a complex function of applied bias, induced optical field strength, and gap size. Furthermore, these results demonstrate that Tien-Gordon tunneling and Fowler-Nordheim Field Emission are defined by the same physical process, explained by the WKB model. By using ac trapping techniques and DNA linked Ag nanocube dimers, single molecule circuits can be constructed that may be used in follow up studies that seek to understand ultrafast electron transport in single molecule circuits using ultrafast dc pulses.

References

1. R. Corkish, M.A. Green, T. Puzzer, “Solar energy collection by antennas,” Sol. Energy. 73, 395-401 (2002).

2. J.G. Simmons, “Generalized formula for the electric tunnel effect between similar electrodes separated by a thin insulating film,” J. Appl. Phys. 43, 1793-1803 (1963).

3. R.H. Fowler, L. Nordheim, “Electron emission in intense electric fields,” Proc. R. Soc. A. 19, 173-181 (1928).

4. J.W. Gadzuk, E.W. Plummer, “Field emission in intense electric fields,” Rev. Mod. Phys. 45, 487-548 (1973).

5. A.A. Lucas, P.H. Cutler, T.E. Feuchtwang, T.T. Tsong, T.E. Sullivan, Y. Yuk, H. Nguyen, P.J. Silverman, “Use of a scanning tunneling microscope to rectify optical frequencies and measure an operational tunneling time,” J. Vac. Sci. Technol. A. 6, 461-465 (1988).

6. A.V. Bragas, S.M. Landi, O.E. Martinez, “Laser field enhancement at the scanning tunneling microscope junction measured by optical rectification,” Appl. Phys. Lett. 72, 2075-2077 (1998).

7. J.R. Tucker, “Quantum limited detection in tunnel junction mixers,” IEEE J. Quantum Electron. 15, 1234-1258 (1979).

8. D.R. Ward, F. Huser, F. Pauly, J.C. Cuevas, D. Natelson, “Optical rectification and field enhancement in a plasmonic nanogap,” Nat. Biotechnol. 5, 732-736 (2010).

9. R. Arielly, A. Ofarim, G. Noy, Y. Selzer, “Accurate determination of plasmonic fields in molecular junctions by current rectification at optical frequencies,” Nano Lett. 11, 2968-2972 (2011).

10. S. Dey, D. Mirell, A.R. Perez, J. Lee, V.A. Apkarian, “Nonlinear femtosecond laser induced scanning tunneling microscopy,” J. Chem. Phys. 138, 154-202 (2013).

11. L. Wu, H. Duan, P. Bai, M. Bosman, J.K.W. Yang, E. Li, “Fowler-Nordheim tunneling induced charge transfer plasmons between nearly touching nanoparticles,” ACS Nano. 7, 707-716 (2013).

12. R. Esteban, A. Zugurramuri, P. Zhang, P. Nordlander, F.J. Garcia-Vidal, A.G. Borisov, J. Aizpurua, “A classical treatment of optical tunneling in plasmonic gaps: extending the quantum corrected model to practical situations,” Faraday Disc. 178, 151-183 (2015).

13. X. Liu, Y. Wang, E.O. Potma, “A dual-color plasmonic focus for surface-selective four-wave mixing,” Appl. Phys. Lett. 101, 081116 (2012).

14. A. Rodriguez Perez, “Ultrafast laser-induced tunneling of electrons on plasmonic tips and nanojunctions,” Ph.D. Dissertation, University of California, Irvine (2013).

15. B. Sharma, R.R. Fronteira, A. Henry, E. Ringe, R.P. Van Duyne, “SERS: Materials, applications, and the future,” Materials Today. 15, 16-22 (2012).

16. K. B. Mogensen, K. Kneipp, “Size-Dependent Shifts of Plasmon Resonance in Silver Nanoparticle Films Using Controlled Dissolution: Monitoring the Onset of Surface Screening Effects,” J. Phys. Chem. C. 118, 28075-28083 (2014).

17. M.W. Knight, N.S. King, L. Liu, H.O. Everitt, P. Nordlander, N.J. Halas, “Aluminum for Plasmonics,” ACS Nano. 8, 834-840 (2014).

18. C. Langhammer, Z. Yuan, I. Zoric, B. Kasemo, “Plasmonic Properties of Supported Pt and Pd Nanostructures,” Nano Lett. 6, 833-838 (2006).

19. B. Albee, X. Liu, F.T. Ladani, R.K. Dutta, E.O. Potma, “Distance-dependent photo-induced electron transport in nanometer-sized junction,” J. Opt. 18, 054004 (2016).

20. C. Xiang, J.Y. Kim, R.M. Penner, “ Reconnectable sub-5 nm nanogaps in ultralong gold nanowires,” Nano Lett. 9, 2133-2138 (2009).

21. S. Yampolsky, D.A. Fishman, S. Dey, E. Hulkko, M. Banik, E.O. Potma, “Seeing a single molecule vibrate through time-resolved coherent anti-Stokes Raman scattering,” Nature Photonics. 8, 650-656 (2013).

22. P.P. Pal, N. Jiang, M.D. Sonntag, N. Chiang, E.T. Foley, M.C. Hersam, R.P. Van Duyne, T. Seideman, “Plasmon-mediated electron transport in tip-enhanced Raman spectroscopic junctions,” J. Phys. Chem. Lett. 6, 4210-4218 (2015).

23. V. Linkko, “DNA-BASED APPLICATIONS IN MOLECULAR ELECTRONICS,” Ph.D. Dissertation, University of Jyvaskyla (2011).

CHAPTER 4: Plasmonic Au Nanostructures for the Enhancement of Magentic Fields at Optical Wavelengths

4.1 Background and Significance

In chapters 2 and 3 we looked at plasmonic Au nanostructures for the enhancement, control, and propagation of electric fields at optical wavelengths. In this chapter, yet again, we will slightly shift our focus to another interesting topic related to Au nanostructures. We will now focus on using plasmonic Au nanomaterials for the enhancement of magnetic fields.

The magnetic component of light is of recent interest to scientists and engineers for several different reasons. In particular, optical magnetic transitions in materials offer a unique set of light-matter interactions. Addressing these transitions allows access to material states and dynamics that are not always directly accessible with electric field mediated transitions to be studied in a controlled manner. Long-lived triplet states can be manipulated with magnetic field interactions, offering novel opportunities for writing and reading memory in units as small as single molecules. Devices that use magnetic fields at optical wavelengths may usher in new materials for the computing industry, including and not limited to, quantum spin-encrypted ultrafast-optical memory.

Despite the exciting potential of optical magnetism, such devices and studies are only recently gaining momentum. This is largely because the expected magnetic field interactions with matter, such as a nanoparticle, are typically significantly weaker than interactions with the

electric field component at optical wavelengths. As a result, optical magnetism is generally difficult to observe in most standard optical lab settings, unlike electric field interactions.

Trivalent lanthanide ions are a notable exception to weak magnetic field interactions. These materials exhibit relatively strong and narrow magnetic dipole allowed transitions in the visible and near-infrared (NIR) range of the spectrum [1-3]. Despite these advancements, enhancement of the interaction of magnetic field with matter is desirable. The latter can be achieved with nanoantennas that are optimized to locally enhance the magnetic field component of light at visible and NIR wavelengths. Only recently have magnetic field plasmonic resonators been examined in the literature, with a wide range of questions left to answer with respect to controlling and maximizing the enhancement of magnetic fields using plasmonic nanostructures [4,5].

Here, we propose a novel set of Au magnetic field nanoresonators for the enhancement and control of local magnetic fields at optical wavelengths. We will explore the fabrication of such structures using Focused Ion Beam (FIB) milling techniques, as well as the spectral responses of the devices in white light scattering experiments. We will also examine the spectra of optically magnetic lanthanide films and nanoparticles, and discuss how these materials can be used in conjunction with our films to measure the enhanced magnetic field of the devices through far field optical imaging using white light scattering.

4.2 Theoretical Predictions for Local Magnetic Field Enhancement

To understand the spectral regime where we expect magnetic field enhancement for the proposed devices, we must first look at theoretical predictions with respect to the proposed

Au nanostructures. The theoretical calculations and expectation discussed in this chapter were calculated with the help of the Capolino Group at UCI. In this chapter, we will focus on one primary structure, Au nanogunbarrels. The geometry for each of these structures is shown in figure 4.1.

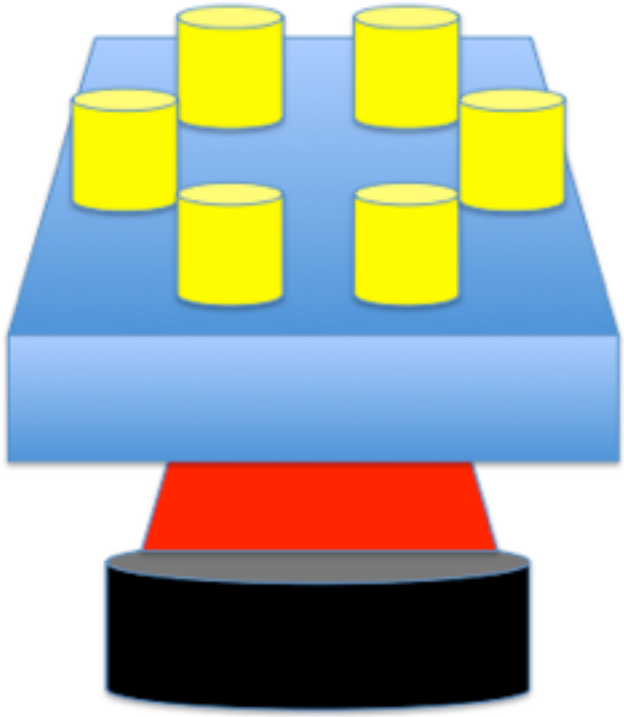

Figure 4.1: Plasmonic Au Nanogunbarrel for the enhancement of magnetic fields at optical wavelengths. The pillars of the structure act as electric field antenna, while the central region is theoretized to enhance magnetic fields at optical wavelengths. Resonance frequencies for magnetic field enhancement in these studies will be examined around 800nm.

As we can see, the structure shows azimuthal-symmetry in the x and y-planes. In addition, the very small distance between pillars in the nanogunbarrel gives rise to an efficient electric field antenna effect, much like the Au and Ag nanoparticle dimers discussed briefly in previous chapters. The azimuthal organization of the gaps introduces an effective electron displacement in a ring around the structure of the pillars, producing a magnetic field normal to the lateral plane in the central region of the gunbarrel structure.

If this structure is excited using light at optical wavelengths, a local magnetic field enhancement is seen at a characteristic wavelength for the device. The resonance wavelength of the devices is tunable over a narrow wavelength range, as is demonstrated in theoretical predications outlined in Figure 4.2. Furthermore, each structure has a different expected resonance wavelength. By changing parameters such as gap size between pillars and radius of pillars the wavelength where the magnetic field is enhanced can be shifted either in the blue or red directions with respect to resonance wavelength. Based on the results of the simulations, it is believed that gap size is a particularly crucial parameter for tuning magnetic field enhancement at optical frequencies.

To demonstrate these concepts theoretically, the expected resonance wavelength for gunbarrel structures with gaps of 10-15nm were simulated, pillar heights of 90nm, and a diameter ranging from 95-100nm. These are parameters were chosen as they are feasible for fabrication using modern FIB milling technology, which can produce features down to 4nm in size depending on the ion gun source. The magnetic field enhancement (H/H_0) expected for a few representative structures is demonstrated in Figure 4.2. The variable parameters (gap size, pillar height, pillar diameter) simulated in this figure represent realistic values based on

structures that have been successfully constructed in the lab using bitmap assisted milling. The expected magnetic field enhancement resonance wavelengths of these devices are between 700-900nm, in the NIR optical regime. The expected magnitude of enhancement ranges from 4.5 (700nm) to 5.5 (900nm). Over this wavelength range, a redshift occurs in the resonance of the device as the gap size is increased. The effects of changing pillar height and diameter are not as strong, indicating the dominant variable that affects the resonance wavelength of magnetic field enhancement in these devices is gap size. Interestingly, the magnetic field enhancement also increases as gap size is likewise increased. Now that we have discussed the theoretical predictions for the resonant magnetic fields for our plasmonic Au nanostructures, we will move on to the experimental focus of this chapter.

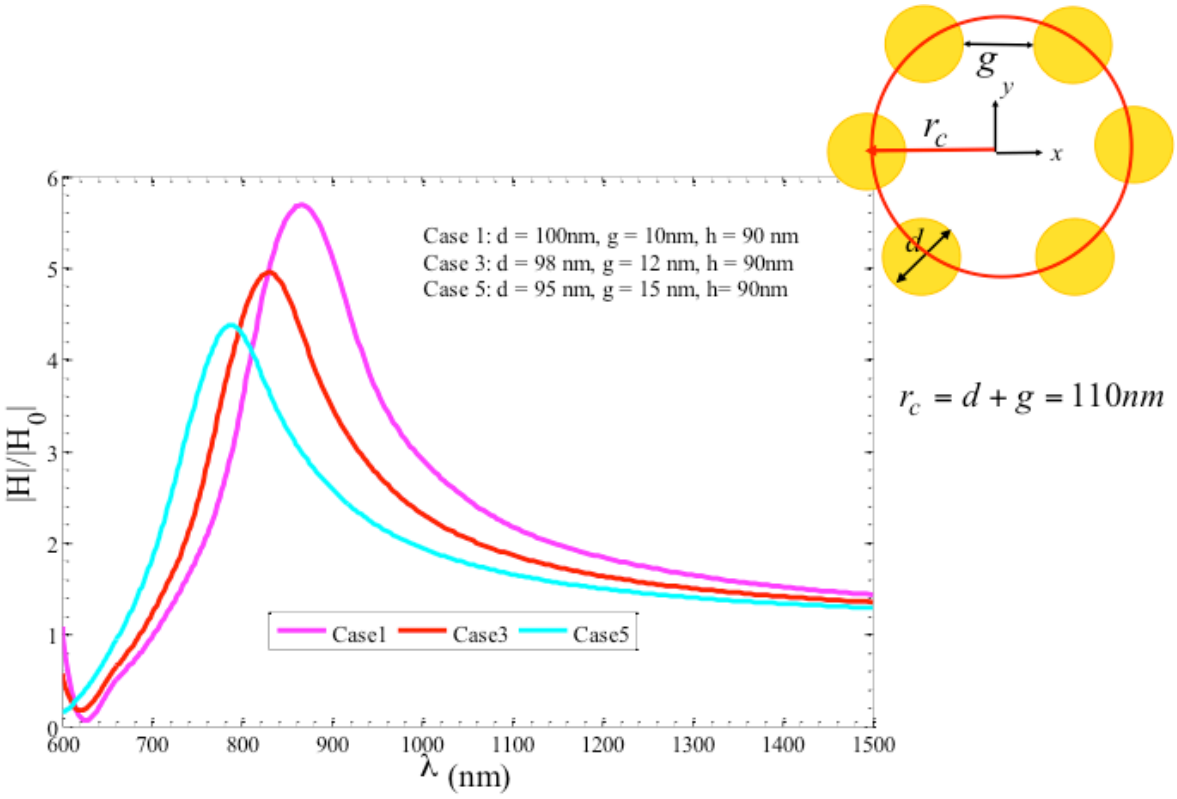

Figure 4.2: The expected magnetic field enhancement wavelength for nanogunbarrel devices as a function of gap size between individual pillars. As demonstrated in this theoretical study, as the gap size is increased, the expected resonance wavelength of the magnetic field enhancement is red shifted, while when it is decreased, a blue shift in the resonance wavelength is expected. The average expected magnetic field enhancement (H/H_0) for the 700-900nm wavelength range is 5. Image provide courtesy of the Capolino Group at UCI.

4.3 Fabrication of Structures

Now that we have laid out a theoretical basis for the enhancement of local magnetic fields in Au plasmonic structures, we will focus on the fabrication of such structures for the examination of these electromagnetic phenomena in a controlled laboratory setting for verification. The process used to fabricate the structures described below is pictorially demonstrated in Figure 4.3. The fabrication process can be broken down into three key steps: thermal deposition of Au thin-films, bitmap assisted FIB Milling of the desired structure, and SEM characterization of the final product.

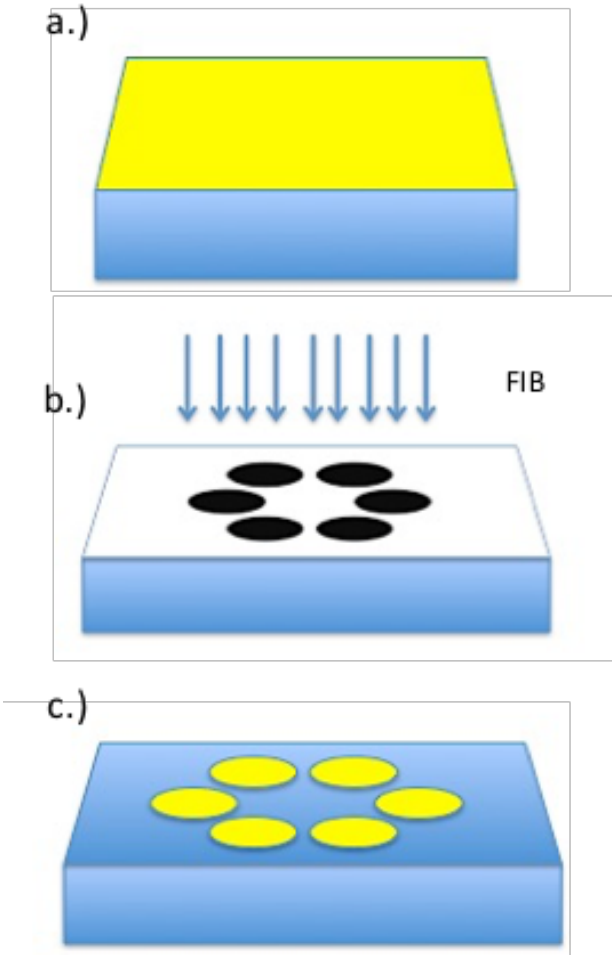

Figure 4.3: Fabrication process of the nanogunbarrel magnetic resonators. a.) A 100nm thin-film of gold is first thermally evaporated onto the surface of a thin glass cover slip. b.) After deposition, a bitmap assisted FIB milling procedure is performed to directly write c.) the desired gunbarrel structure from the film.

4.3.1 Thermal Deposition of Gold Films

To begin the fabrication process for the Au nanogunbarrels, thin films of Au were prepared to use as milling templates in subsequent steps. All films were prepared using a Denton High Vacuum thermal deposition setup. For the fabrication of nanogunbarrels, a 100nm thick film was prepared. To thermally coat the films, thin cover glass from Fisher Scientific was precleaned by sonicating the glass slides in ethanol for 20min, followed by acetone for 20min, followed by nanopure water for 20min. Once cleaned, the slides were air dried with nitrogen prior to thermal deposition of the Au thin-films. To promote optimal adhesion of the Au tin-film to the glass cover slips, a 2nm Cr adhesion layer was thermally evaporated first during thermal evaporation, followed by the Au thin-film layer. After application of the Au thin-films using thermal evaporation, the slides were stored under vacuum to prevent any contamination from the local environment until subsequent milling steps.

4.3.2 Direct Bitmap Assisted Focused Ion Beam Milling of Au Nanogunbarrels

To prepare the Au nanogunbarrels structures needed to enhance and optically excite the desired magnetic fields, a consistent and high-resolution fabrication technique is required. Achieving the feature sizes dictated by theoretical studies is a challenging endeavor. To enhance magnetic fields to a magnitude that is detectable using plasmonic Au nanogunbarrels, gaps between electric field antenna components within the greater structures (i.e. the pillars or nanobullets) must be engineered down to sizes of 10-15nm in the smallest cases. To achieve

this resolution, a FEI Quanta 3d SEM/FIB was used to mill the desired structures into the gold films prepared using thermal evaporation.

To achieve a high rate of fabricated structures and easily tune the size and therefore expected resonance wavelength of the structure, a bitmap assisted milling procedure was performed to automate the fabrication process of the desired gunbarrels, as this feature was equipped as a fabrication option on the Quanta 3d used for experiments. To perform this milling procedure, a black/white bitmap representing an array of the structures was prepared using Adobe Illustrator. In the native driver software for the Quanta 3d SEM/FIB, white portions of the bitmap prepared are milled while black portions are left behind by blanking the beam in these coordinates during milling. To achieve optimal resolution in our devices a milling beam current of 27pA was used, with an accelerating voltage of 30keV. Furthermore, the images were prepared in a 4”x4” window, with a 1” = 1 micron (1pixel/nm) image scaling factor. The example bitmap array used to produce all gunbarrels is detailed further in Figure 4.4.

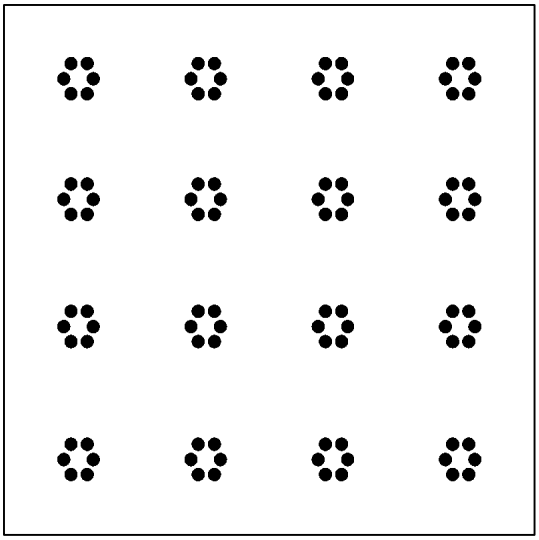

Figure 4.4: Bitmap array used to mill nanogunbarrels into gold films during milling procedures. To achieve the resolution required to fabricate the smallest cases, a 1' = 1um, 1px = 1nm relationship was used in production of the bitmap used for milling. White areas of the bitmap are automatically milled by the Quanta 3d used in fabrication, and black areas are blanked to be left behind.

4.3.3 SEM Characterization of Structures

SEM images of the fabricated structures for the desired nanogunbarrels are shown in Figure 4.5. As we can see for the nanogunbarrels, a wide range of tunable sizes can be achieved using bitmap-assisted FIB milling to directly "draw" the desired structures into gold films. This serves an advantage over competing methods of fabrications such as Electron Beam Lithography (EBL). Although the structures can also be written into PMMA films and produced by means of a further chemical exposure and lift-off procedure, the additional chemical steps and processing involved are not as efficient as a direct FIB milling of the structures into a gold film.

Despite success in fabricating devices with the desired features for magnetic field enhancement in the NIR optical regime, there is a trade-off to using bitmap assisted FIB milling as a means of simplifying high throughput processing of said devices. Namely, even though the desired structures are produced with a high degree of precision, remnant gold deposited on and around the structures during milling makes many devices produced unusable for the enhancement of magnetic fields at optical wavelengths. Despite this cost, structures with pillar diameters down to 15nm could be fabricated at a success rate of 30% using this fabrication method. Larger structures could be produced with similar precision, with gap sizes on the order of 30nm. These devices were constructed with a gallium ion beam that is reported by FEI to have a fabrication resolution around 10nm. Future work with a helium beam and similar bitmap assisted FIB procedures could be performed to improve device fabrication success rates. Similarly, EBL production of such structures could be pursued to achieve structures, though it is difficult to do with high success rates at the described device thickness (100nm). This is largely

because doing so requires a PMMA film thickness at least 2-3 times greater than the height of the pillars in the fabricated gunbarrels to perform lift-off fabrication at the desired scales (100nm pillar diameter, 15nm gap, 100nm height). As a result, a high failure rate occurs in writing, developing, and filling-in structures using this process. To perform this type of fabrication, the height of the pillars in the devices must be significantly decreased to allow for realistic thicknesses of PMMA films used for lift-off fabrication of such structures.

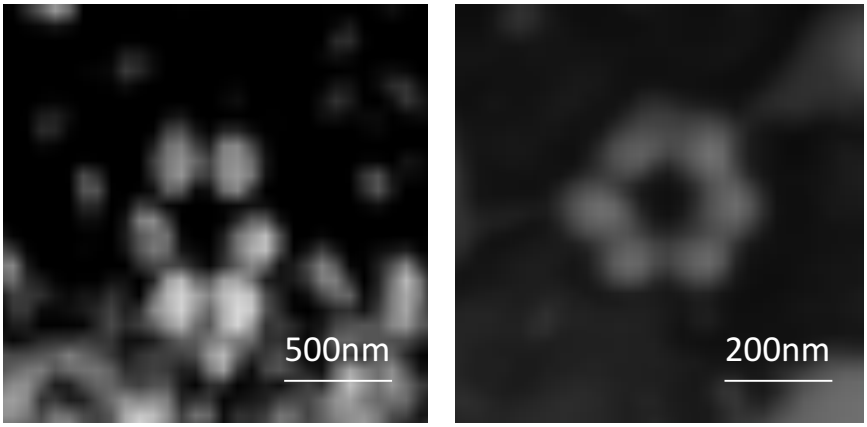

Figure 4.5: Single SEM Images of gunbarrels fabricated using bitmap assisted FIB milling. As demonstrated, structures can be fabricated over a variety of sizes allowing for the tuning of the resonance magnetic field enhancement wavelength depending on size as predicted by theoretical studies provided by the Capolino group at UCI.

As seen in the SEM images of the fabricated devices, the gunbarrels were fabricated to be positive templates with respect to Au over a range of sizes, allowing for tuning of the expected magnetic resonance wavelength in the devices. For these structures, the templates could be produced reproducibly to scale using bitmap assisted milling procedures.

4.4 Trivalent Lanthanide-Rich Materials as a Probe for Optical Magnetic Fields

To further characterize the electromagnetic behavior of the devices in a meaningful manner, care must be taken in performing optical measurments. As the expected magnetic resonance of the Au nanogunbarrels is based on theory, it is not certain that a resonance will occur at the exact wavelength predicted by theory. To ensure that the experimental observation of the resonance is in line with theory, and vice versa, a reliable method of probing magnetic excitations at optical wavelengths must be devised. A possible route toward the development of a nanoprobe for magnetic fields is the fabrication of a scan probe tip coated with a material that exhibits strong magnetic transitions in the visible and NIR ranges of the spectrum.

4.4.1 Probes for Magnetic Field Enhancement at Visible and NIR Wavelengths

Materials enriched with trivalent lanthanide ions are a relevant family of materials with appreciable magnetic dipole allowed optical transition. This is because the trivalent ions of this family have unpaired electrons in f-orbitals, affected by relatively strong spin-orbit coupling. Magnetic moments of these electrons are determined by both spin and orbital momenta. Furthermore, electrons in the lanthanide f-orbitals are shielded by nearby p-orbitals. This in

turn, gives rise to a relatively small crystal field splitting effect and weak coupling to molecular vibrations. Consequently, electronic transitions between f-orbital states are relatively weak in intensity, and narrow in bandwidth. In principle, the Laporte Rule forbids electric dipole transitions between f-orbital states. As a result, a higher prominence is given to magnetic dipole and multipole transitions between these states.

Judd-Ofelt Theory has been used to theoretically calculate both the energy levels, and allowed magnetic dipole and electric quadrupole contributions of f-orbital transitions. Tables 4.1 and 4.2, summarize the expected wavelengths of magnetic dipole absorption in lanthanides according to Dodson et. al [6]. To move toward nanosystems capable of probing localized magnetic field optically using the fabricated gold nanostructures, we will now discuss a series of experiments focused on better understanding the experimental spectra of several lanthanide ion species that can be placed in the fabricated structures to probe magnetic field enhancement in the lab, compared to theoretically predicted results, allowing for tuning of the magnetic field probe to fit the resonance of a given fabricated gunbarrel. In addition, we will explore an interesting case of optical scattering in Er_2O_3 nanoparticles that shows evidence of a magnetic resonance.

Lanthanide Ion	Absorption Wavelength (nm)	Magnetic Dipole (MD) or Electric Quadrupole (EQ)
Er^{3+}	366	MD
	450	EQ
	500	EQ

Table 4.1: Theoretically predicted absorption wavelengths for magnetic dipole and electric quadrupole modes for Er^{3+} ions. Values provided in the table were taken from Dodson et. Al. [6].

Lanthanide Ion	Absorption Wavelength (nm)	Magnetic Dipole (MD) or Electric Quadrupole (EQ)
Nd^{3+}	340	MD
	515	EQ
	592	MD
	688	MD
	822	MD

Table 4.2: Theoretically predicted absorption wavelengths for magnetic dipole and electric quadrupole modes for Nd^{3+} ions. Values provided in the table were taken from Dodson et. Al. [6].

4.4.2 Preparation of Er-Triflate and Nd-Triflate Films

To prepare a suitable Ln^{3+} ion containing material that may be placed in fabricated Au nanostructures with detectable, magnetic dipole allowed absorption and emission, a series of Ln-Triflate films were prepared in collaboration with the Evans group at UCI.

To determine the optimal conditions for coating and ensure an even distribution of the solution prepared by collaborators, a test was first performed comparing spin coating with drop casting for a concentration range of the Ln^{3+} species of interest (Ln = Er, Nd). The concentration range with respect to Ln-Triflate in solution for casting was .25% to 1% by weight.

To prepare the spin-coated samples, clean glass cover slips were placed on a commercial tabletop spin coater, preprogrammed to spin at a rate of 1500RPM. Samples were spun for a total time of 1min/sample, until dry, and stored under vacuum until spectral analysis to minimize potential contamination from the local environment.

To prepare the drop cast samples, a thin, continuous layer of solution was placed on clean glass cover slips and allowed to air dry before spectral analysis. Once dry, the samples were also stored under vacuum to ensure minimal contamination from the local environment prior to spectral analysis.

A continuous, uniform film was achievable for the Er-Triflate and Nd-Triflate samples tested, when drop cast and air dried. As a result, Er-Triflate and Nd-Triflate are good candidate compounds for testing magnetic field enhancement in the fabricated nanostructures from a uniform coverage perspective. The inclusion of these materials into future fabrications will allow for optical experiments that discriminate between magnetic field excitations on a

resonator and off, effectively measuring magnetic field enhancement in Au nanostructures of interest through a far field magnetic dipole imaging measurement.

4.4.3 Spectral Analysis of Ln^{3+} Ion Containing Films

To understand the spectral lines that may be targeted using the above described devices for enhanced excitation and emission of magnetic dipoles using Ln-Triflate films, absorption spectra were performed to get a profile of the experimental magnetic field dipole excitation wavelengths of the relevant species of Ln-Triflate films, and compare the experimentally determined results to theoretical predictions performed using Judd-Ofelt Theory [6,7].

Due to the best film quality coverage in initial film deposition tests being found in Er-Triflate and Nd-Triflate, only absorption spectra for these species will be examined. To perform the absorbance spectra, a Cary-50 UV-Vis Spectrometer was used, fitted with an adapted mount for film measurements. Sample absorption spectra for these two species is detailed in Figure 4.6. As demonstrated in the spectra, the experimentally obtained spectra for Er-Triflate and Nd-Triflate match the theoretically predicted spectral lines very well. Future experiments will be performed to determine the expected experimental emission lines from these experimentally determined excitation modes for these lanthanide species. Interestingly, we also see the rise of lines with the expected character of magnetic dipoles that are not predicted in literature for Er-Triflate. In these films, a sharp mode is consistently visible at 650nm as well as a very weak, sharp mode at 795nm. Theoretical predictions suggest the existence of real states that allow for the excitation magnetic dipoles and higher order octupoles respectively at these wavelengths [7].

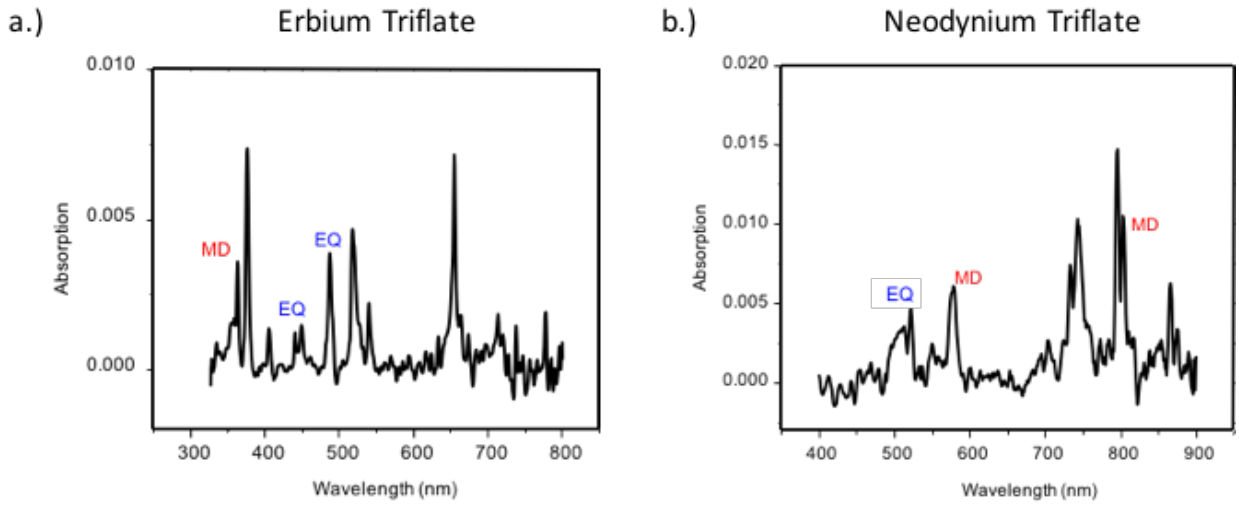

Figure 4.6: The representative absorption spectrum for a thin film of a.) Er Triflate and b.) Nd Triflate drop cast onto glass cover slips. Spectra were acquired using a Cary 50 UV-Vis spectrometer. As demonstrated in the spectrum, sharp, weak spectral lines characteristic of magnetic dipoles (ND) and electric quadrupoles (EQ) can be seen in accordance with theoretically predicted lines.

The observation of these generally forbidden transitions is likely a result of symmetry breaking in the Ln^{3+} ions bound to triflate in the films. Heavy spin-orbit coupling in the Ln^{3+} ions is a generally well accepted source for relaxation of quantum selection rules in this family of luminescent molecules as well, which may further explain the observations in the spectra acquired. Our studies of Ln^{3+} triflate films confirm previous spectroscopic measurements of lanthanide rich materials and highlights their use as easy-to-handle probes with discernable magnetic transitions in the visible range of the spectrum.

4.4.4 Er_2O_3 Nanoparticles and Magentic Field Enhancement

To better understand magnetic dipole resonance in a wider range of Er^{3+} containing materials, a .1% by wt solution of Er_2O_3 nanoparticles (~100nm, Sigma Aldrich) was suspended in nanopure water using a bath sonicator at room temperature for 15min and filtered with a 500nm mesh to ensure large aggregates of particles were largely excluded prior to placement on a clean glass cover slip. Once filtered, a thin layer of solution was placed on a clean glass cover slip and the particles were spin-coated onto the glass at a rate of 1500rpm until dry to ensure a disperse, uniform coverage of the particles on the slide. Once dry, the sample was stored under vacuum for later optical measurements.

4.4.5 Optical Signatures of Visible Magnetic Light from Er_2O_3 Nanoparticles

Observations in absorption experiments performed on erbium oxide nanoparticles encased in glass [3] suggest a weak, sharp spectral feature at 795 nm. This excitation is attributed to the $^4I_{15/2}$ -> $^4I_{9/2}$ f-f orbital transition. Due to the weak, narrow nature of the line at

795nm, this mode is hypothesized to contain primarily magnetic or higher order electric multipole contributions (ie. electric and magnetic quadrupole or octupole).

To determine if this resonance could be measured directly in erbium oxide nanoparticles at visible wavelengths, a white light scattering experiment was performed in collaboration with the Apkarian group at UCI. As is demonstrated in Figure 4.7, dark field scattering measurements of a single Er_2O_3 nanoparticle indicate a resonance at 798nm. It is believed that this peak arises from an excitation of the $^4I_{15/2}$ -> $^4I_{9/2}$ transition, as described by Ragin et. al. [3].

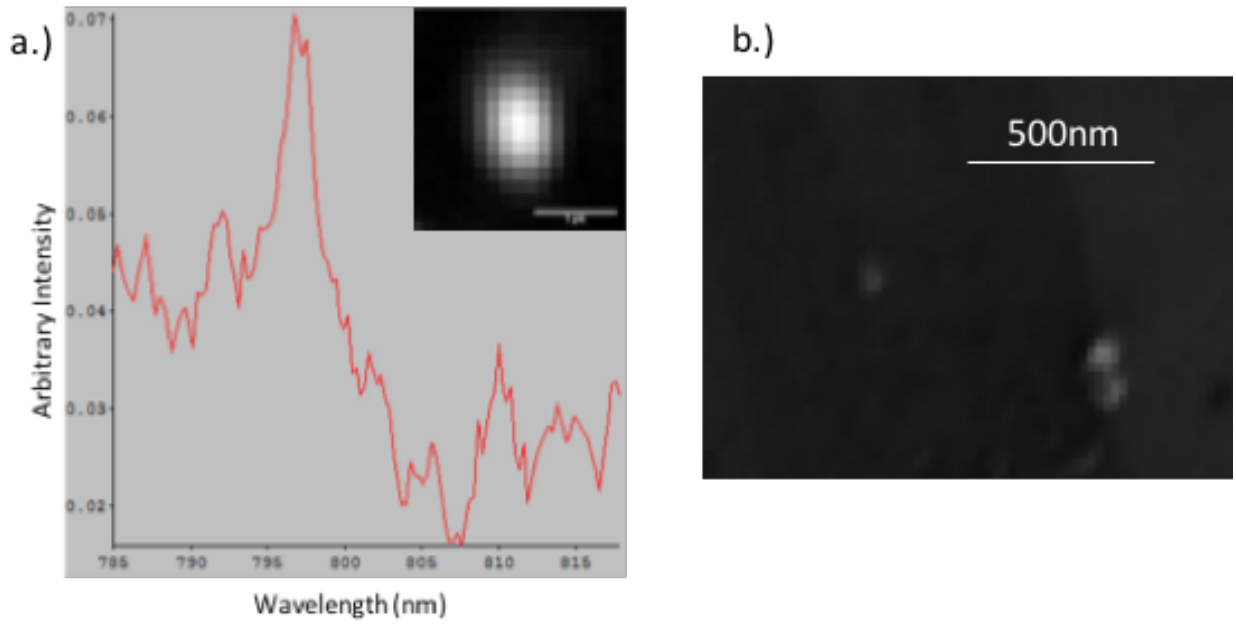

Figure 4.7: a.) The dark field scattering spectrum and image of a single Er_2O_3 nanoparticle acquired courtesy of the Apkarian group at UCI. A look at the spectral region between 785 and 815nm shows a weak, sharp spectral feature characteristic to the signatures given by magnetic modes, suggesting a magnetic excitation resonant at 798nm. b.) A representative SEM image of Er_2O_3 nanoparticles used for optical measurement shows an average particle size around 100nm.

To probe the hypothesized magnetic character of the peak at 798nm in far field scattering measurements, an inverted laser backscattering microscope (Olympus IX71) was adapted to excite the erbium oxide particles with 800nm ultrafast source (Coherent Mira 900, 800nm, 150fs, 80MHz) in the epi-direction. To map the scattering efficiency as a function of sample position, a piezo scanning stage was fitted to the microscope (Mad City Labs, Nano-XYZ) and controlled through a homebuilt LabVIEW program to perform saw-scan image collections of the field scattered by the particles in the epi-direction of the microscope. A photomultiplier tube (Hamamatsu) was used to measure the intensity of the scattered field collected during imaging. Finally, an azimuthal polarizer (ArcOptix) was placed in the setup to illuminate the particles with a focused, azimuthally polarized beam. The focus of such a beam contains a central region dominated by the magnetic field, surrounded by a "donut" of electric field. An image of the microscope and scattering images obtained with this setup are detailed in Figure 4.8.

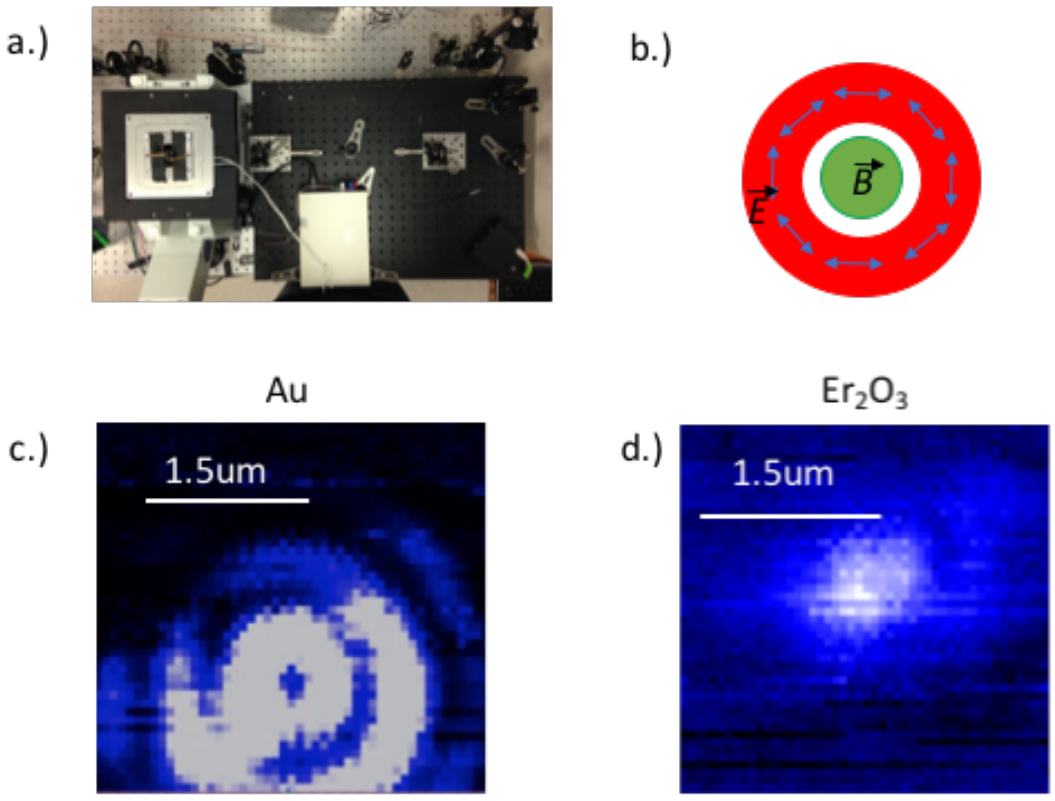

Figure 4.8: a.) Backscattering microscope constructed to image b.) azimuthally polarized beams scattered in the epi-direction from c.) 20nm AuNPs and 100nm Er_2O_3 NPs. As demonstrated in the images, the donut shape of the scattered far-field of the AuNP indicates dominant electric field scattering as the region of highest intensity over the scanned area is found in the electric field ring of the APB. In contrast, the Er_2O_3 NP shows the highest intensity in the center of the APB spot where the magnetic field is highest. This measurement suggests a dominant magnetic nature of the scattering spectrum acquired near 800nm.

As demonstrated in the images, when imaging a single Er_2O_3 nanoparticle using an APB, the largest intensity of the scattered field using is seen in the central region of the beam, in the region where electric field is minimal and magnetic field is expected to be greatest. This suggests a magnetic signature to the peak at 798nm seen in scattering experiments, in line with observations made by Novotny et. al measuring the magnetic and electric field scattering profiles using Eu^{3+} doped Yb_2O_3 nanoparticles [8]. To verify this observation further, the experiment was repeated using Au nanoparticles, which do not display a strong magnetic resonance at the chosen excitation wavelength. In the case of Au nanoparticles when excited with an APB, the maximum intensity of the imaged field enhancement is in the donut region of the beam where electric field is expected to be maximum, with no measureable increase in intensity in the central region of the beam, where the magnetic field of the APB is maximum.

Further work is required to better understand the physical origin of the scattering measurements on Er_2O_3 nanoparticles. However, a pump-probe excitation of the $^4I_{15/2}$ -> $^4I_{9/2}$ state is hypothesized, in line with observations reported in recent literature [3]. This state is suggested by quantum selection rules to be a magnetic quadrupole or octupole. Our measurements suggest a possible magnetic origin of the 798nm resonance, spurring further examination of Er_2O_3 and other lanthanide oxide nanoparticles as an additional variety of magnetic field probes at visible and NIR wavelengths.

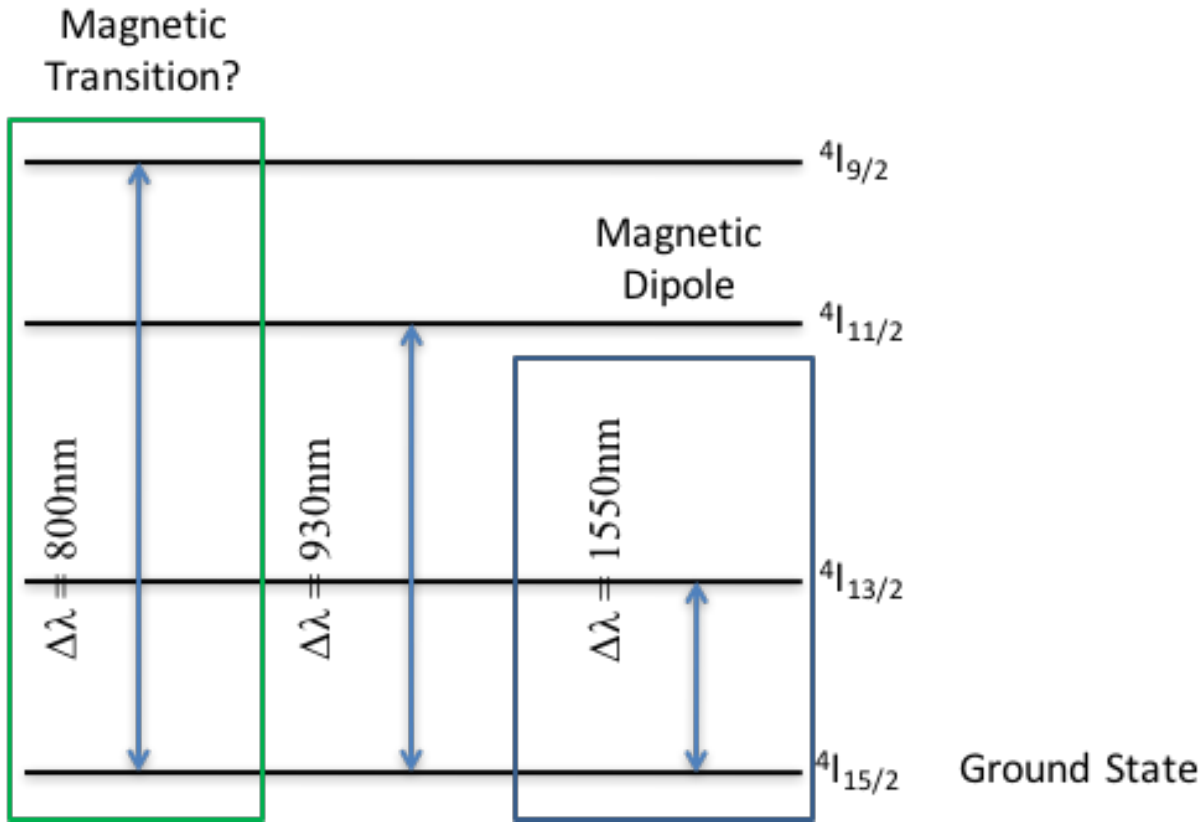

Figure 4.9: Theoretical energy level diagram of Er^{3+} as predicted by Judd-Ofelt Theory [9]. The profile of backscattering images acquired for a single Er_2O_3 using azimuthally polarized light near 800nm are hypothesized to result from a transition of the $^4I_{15/2}$ ground state electron to the $^4I_{9/2}$ state [3]. The single spot profile of the backscattering image acquired in a single Er_2O_3 nanoparticle using azimuthally polarized light indicates a magnetic nature to this transition.

4.5 Closing Remarks

In this chapter, we described the fabrication of Au nanostructures for enhancing and controlling magnetic fields at optical wavelengths. As demonstrated, bitmap assisted focused ion beam (FIB) milling can be used to reliably construct nanogunbarrel devices directly from Au thin films.

The absorption spectra of various Ln^{3+} Ion containing films were examined as candidate reporters of far-field measurements of enhanced magnetic fields in the fabricated structures in optical measurements at visible and NIR wavelengths. The spectra elucidate experimental values for MD and EQ modes that have been theorized in the literature. These modes can be targeted for excitation wavelengths probing the enhanced magnetic field in fabricated Au nanogunbarrels in future work.

Finally, we demonstrate direct magnetic pump-probe imaging using Er_2O_3 nanoparticles. A comparative measurement of backscattering images of AuNPs and the pump-probe images of Er_2O_3 NPs near 800nm using an Azimuthally Polarized Beam (APB), suggest a magnetic character to the excitation used to image erbium oxide nanoparticles. The origin of this magnetic character is not yet fully clear, although it is hypothesized to result from an allowed magnetic excitation (quadrupole or octupole) from the $^4I_{15/2}$ ground state to the $^4I_{9/2}$ excited state. This normally forbidden transition, is believed to be allowed due to heavy spin-orbit coupling of the Er^{3+} ions in the particles, as well as symmetry breaking of the particles due to encapsulation in a refractive index matching liquid during measurements.

References

1. T.H. Taminau, S. Karaveli, N.F. van Hulst, R. Zia, “Quantifying the magnetic nature of light emission,” Nat. Commun. 3, doi:10.1038/ncomms1984 (2012).

2. M. Decker, I. Staude, I.I. Shishkin, K.B. Samusev, P. Parkinson, V.K.A. Sreenivasan, A. Minovich, A.E. Miroshnichenko, A. Zvyagin, C. Jagadish, D.N. Neshev, Y.S. Kivshar, “Dual-channel spontaneous emission of quantum dots in magnetic metamaterials,” Nat. Commun. 4, doi:10.1038/ncomms3949 (2013).

3. T. Ragin, J. Zmojda, M. Kochanowicz, D. Dorosz, “Spectroscopic properties of heavy metal oxide glasses doped with Er^{3+} ions,” Photonics Letters of Poland, 7, 38-40 (2015).

4. R. Hussain, S.S. Kruk, C.E. Bonner, M.A. Noginov, I. Staude, Y.S. Kivshar, N. Noginova, D.N. Neshev, “Enhancing Eu^{3+} magnetic dipole emission by resonant plasmonic nanostructures,” Opt. Lett. 40, 1659-1662 (2015).

5. N. Noginova, R. Hussain, M.A. Noginov, J. Vella, A. Urbas, “Modification of electric and magnetic dipole emission in anisotropic plasmonic systems,” Opt. Express. 21, doi:10.1364/OE/21.023087 (2013).

6. C.M. Dodson, R. Zia, “Magnetic dipole and electric quadrupole transitions in the trivalent lanthanide series: Calculated emission rates and oscillator strengths,” Phys. Rev. B. 86, 125102 (2012).

7. R. Reisfeld, “Optical Properties of Lanthanides in Condensed Phase, Theory, and Applications,” Mater. Sci. 2, 37-60 (2015).

8. M. Kasperczyk, S. Person, D. Ananias, L.D. Carlos, L. Novotny, “Excitation of Magnetic Dipole Transitions at Optical Frequencies,” Phys. Rev. Lett. 114, 163903 (2015).